



**NAVAL
POSTGRADUATE
SCHOOL**

MONTEREY, CALIFORNIA

THESIS

**RESONANT TERAHERTZ ABSORPTION USING
METAMATERIAL STRUCTURES**

by

Allan T. Phillips

December 2012

Thesis Advisor:

Co-Advisor:

Second Reader:

Gamani Karunasiri

Fabio Alves

James H. Newman

Approved for public release; distribution is unlimited

THIS PAGE INTENTIONALLY LEFT BLANK

REPORT DOCUMENTATION PAGE
Form Approved OMB No. 0704-0188

Public reporting burden for this collection of information is estimated to average 1 hour per response, including the time for reviewing instruction, searching existing data sources, gathering and maintaining the data needed, and completing and reviewing the collection of information. Send comments regarding this burden estimate or any other aspect of this collection of information, including suggestions for reducing this burden, to Washington Headquarters Services, Directorate for Information Operations and Reports, 1215 Jefferson Davis Highway, Suite 1204, Arlington, VA 22202-4302, and to the Office of Management and Budget, Paperwork Reduction Project (0704-0188) Washington, DC 20503.

1. AGENCY USE ONLY (Leave blank)	2. REPORT DATE December 2012	3. REPORT TYPE AND DATES COVERED Master's Thesis
4. TITLE AND SUBTITLE RESONANT TERAHERTZ ABSORPTION USING METAMATERIAL STRUCTURES		5. FUNDING NUMBERS
6. AUTHOR(S) Allan T. Phillips		
7. PERFORMING ORGANIZATION NAME(S) AND ADDRESS(ES) Naval Postgraduate School Monterey, CA 93943-5000		8. PERFORMING ORGANIZATION REPORT NUMBER
9. SPONSORING /MONITORING AGENCY NAME(S) AND ADDRESS(ES) N/A		10. SPONSORING/MONITORING AGENCY REPORT NUMBER

11. SUPPLEMENTARY NOTES The views expressed in this thesis are those of the author and do not reflect the official policy or position of the Department of Defense or the U.S. Government. IRB Protocol number N/A .

12a. DISTRIBUTION / AVAILABILITY STATEMENT Approved for public release; distribution is unlimited	12b. DISTRIBUTION CODE
---	-------------------------------

13. ABSTRACT (maximum 200 words)

The Sensor Research Lab at the Naval Postgraduate School is developing a real-time THz imaging camera. Vital to its design is the metamaterial absorbing layer (metafilm) within each pixel that allows for THz absorption. While there are numerous applications in the THz region, sensors and sources for THz energy have much room for improvement. The use of metamaterial technology for the purpose of a THz sensor has the potential to reduce costs while greatly improving sensitivity performance. The Sensor Research Lab has fabricated metafilms capable of near 100 percent absorption. In this research project, absorption characteristics of a set of metamaterials were measured using Fourier transform THz spectroscopy and modeled using an RLC circuit. The model provides a good description of the absorption characteristics and should assist in better understanding of the electromagnetic interactions within the metafilm.

14. SUBJECT TERMS Terahertz, THz, Metamaterial, Metafilm		15. NUMBER OF PAGES 77	
16. PRICE CODE			
17. SECURITY CLASSIFICATION OF REPORT Unclassified	18. SECURITY CLASSIFICATION OF THIS PAGE Unclassified	19. SECURITY CLASSIFICATION OF ABSTRACT Unclassified	20. LIMITATION OF ABSTRACT UU

THIS PAGE INTENTIONALLY LEFT BLANK

Approved for public release; distribution is unlimited

**RESONANT TERAHERTZ ABSORPTION USING METAMATERIAL
STRUCTURES**

Allan T. Phillips
Lieutenant, United States Navy
B.S., United States Naval Academy, 2006

Submitted in partial fulfillment of the
requirements for the degree of

MASTER OF SCIENCE IN PHYSICS

from the

NAVAL POSTGRADUATE SCHOOL
December 2012

Author: Allan T. Phillips

Approved by: Dr. Gamani Karunasiri
Thesis Advisor

Dr. Fabio Alves
Thesis Co-Advisor

Dr. James H. Newman
Thesis Second Reader

Dr. Andres Larraza
Chair, Department of Physics

THIS PAGE INTENTIONALLY LEFT BLANK

ABSTRACT

The Sensor Research Lab at the Naval Postgraduate School is developing a real-time THz imaging camera. Vital to its design is the metamaterial absorbing layer (metafilm) within each pixel that allows for THz absorption. While there are numerous applications in the THz region, sensors and sources for THz energy have much room for improvement. The use of metamaterial technology for the purpose of a THz sensor has the potential to reduce costs while greatly improving sensitivity performance. The Sensor Research Lab has fabricated metafilms capable of near 100 percent absorption. In this research project, absorption characteristics of a set of metamaterials were measured using Fourier transform THz spectroscopy and modeled using an RLC circuit. The model provides a good description of the absorption characteristics and should assist in better understanding of the electromagnetic interactions within the metafilm.

THIS PAGE INTENTIONALLY LEFT BLANK

TABLE OF CONTENTS

I.	INTRODUCTION.....	1
	A. METAMATERIAL ABSORBERS	1
	B. USES OF TERAHERTZ TECHNOLOGY.....	2
	C. APPLICATIONS OF TERAHERTZ TECHNOLOGY IN SPACE	4
	D. DISCUSSION OF RESEARCH	5
	E. BENEFITS OF RESEARCH.....	8
II.	DATA COLLECTION & ANALYSIS.....	9
	A. DATA COLLECTION PROCESS & METHODS USED	9
	1. Operation of the FTIR.....	9
	2. Setup of the FTIR.....	10
	3. Parameters for Data Collection	11
	B. PRESENTATION OF DATA COLLECTED & ANALYSIS	13
	1. Varying Square Size	13
	2. Varying Square Period	23
III.	MODELING USING AN RLC CIRCUIT.....	29
	A. RLC CIRCUIT ANALYSIS.....	29
	B. RLC MODEL IMPLEMENTATION AND COMPARISON	31
	1. Relating Capacitance to Square Size.....	32
	2. Relating Resistance to Fill Factor.....	34
	3. Relating Resistance to SiO ₂ Thickness.....	36
	4. RLC Circuit Values Necessary for Modeling Experimental Data	39
	C. RLC MODEL CONCLUSIONS.....	48
IV.	CONCLUSION	49
	APPENDIX A	51
	LIST OF REFERENCES	55
	INITIAL DISTRIBUTION LIST	57

THIS PAGE INTENTIONALLY LEFT BLANK

LIST OF FIGURES

Figure 1.	Metamaterial cell (a) and periodic array of cells (b) from [4].	2
Figure 2.	Micrograph of the metamaterial-based THz bi-material sensor array under development in the Sensor Research Lab at the Naval Postgraduate School. (a) Partial view of the array; (b) zoom of a single pixel.	6
Figure 3.	COMSOL analysis of bi-material sensor with THz metafilm from [2].	6
Figure 4.	Wafer with 25 different metamaterial configurations.	7
Figure 5.	Schematic diagram of a Fourier Transform Infrared Spectrometer.	9
Figure 6.	Schematic of the experimental configuration used for measuring the reflection (a) and transmission (b). The incidence angle (θ) is 15° for both configurations.	10
Figure 7.	Experimental bench setup in OMNIC displaying key parameters for data collection.	12
Figure 8.	Experimental setup in AutoPRO displaying key parameters for data collection.	12
Figure 9.	THz absorption of a metafilm with constant square period of $21\text{ }\mu\text{m}$, varying square size, and SiO_2 layer thickness of $0.4\text{ }\mu\text{m}$.	14
Figure 10.	THz absorption of a metafilm with constant square period of $21\text{ }\mu\text{m}$, varying square size, and SiO_2 layer thickness of $0.8\text{ }\mu\text{m}$.	14
Figure 11.	THz absorption of a metafilm with constant square period of $21\text{ }\mu\text{m}$, varying square size, and SiO_2 layer thickness of $1.2\text{ }\mu\text{m}$.	15
Figure 12.	THz absorption of a metafilm with constant square period of $21\text{ }\mu\text{m}$, varying square size, and SiO_2 layer thickness of $1.6\text{ }\mu\text{m}$.	15
Figure 13.	Peak absorption increases as SiO_2 thickness increases for varying square size with constant square period of $21\text{ }\mu\text{m}$. Data points are fitted with an exponential fit for clarity of trend using the equation $y = y_0 + Ae^{R_0x}$.	16
Figure 14.	Peak absorption frequency shifts as a function of square size with constant square period of $21\text{ }\mu\text{m}$. Data points are fitted with an exponential fit for better observation of trending behavior using equation $y = y_0 + Ae^{R_0x}$.	17
Figure 15.	Peak absorption frequency shifts as a function of inverse square size with constant square period of $21\text{ }\mu\text{m}$. Data points are fitted with a linear fit.	18
Figure 16.	Full width half maximum (FWHM) shifts as a function of square size with constant square period of $21\text{ }\mu\text{m}$. Data points are fitted with an exponential fit for better observation of trending behavior using equation $y = y_0 + Ae^{R_0x}$.	19
Figure 17.	Full width half maximum (FWHM) shifts as a function of inverse square size with constant square period of $21\text{ }\mu\text{m}$. Data points are fitted with a linear fit.	19
Figure 18.	Quality Factor, defined as resonant frequency divided by FWHM, as a function of square size with constant square period of $21\text{ }\mu\text{m}$. Data points are fitted with a linear fit. In the case of the $1.6\text{ }\mu\text{m}$ SiO_2 , the last data point is ignored.	20

Figure 19.	Peak absorption as a function of fill factor where square period remains constant at 21 μm . Data points are fitted with an exponential fit for clarity of trend using equation $y = y_0 + Ae^{R_0x}$	21
Figure 20.	Peak absorption as a function of inverse fill factor where square period remains constant at 21 μm . Data fitted with a linear fit.....	22
Figure 21.	THz absorption of a metafilm with varying square period, constant square size of 16 μm , and SiO_2 layer thickness of 0.4 μm	23
Figure 22.	THz absorption of a metafilm with varying square period, constant square size of 16 μm , and SiO_2 layer thickness of 0.8 μm	24
Figure 23.	THz absorption of a metafilm with varying square period, constant square size of 16 μm , and SiO_2 layer thickness of 1.2 μm	24
Figure 24.	THz absorption of a metafilm with varying square period, constant square size of 16 μm , and SiO_2 layer thickness of 1.6 μm	25
Figure 25.	Peak absorption increases as SiO_2 thickness increases for varying square period with constant square size of 16 μm . Data points are fitted with an exponential fit for clarity of trend using equation $y = y_0 + Ae^{R_0x}$	26
Figure 26.	Peak absorption as a function of square period with constant square size of 16 μm . Data points are fitted with a linear fit.....	27
Figure 27.	Peak absorption remains nearly constant as a function of square period with constant square size of 16 μm . Data points are fitted with a linear fit.	27
Figure 28.	Peak absorption as a function of fill factor where square size remains constant at 16 μm . Data points are fitted with a linear fit.....	28
Figure 29.	RLC circuit in series with resistance, R, inductance, L, and capacitance, C.	29
Figure 30.	Comparison between an RLC circuit model (red) with $R = 1.07 \Omega$, $L = 0.21 \text{ pH}$, $C = 0.00521 \text{ pF}$ and actual data with Savitzky-Golay smoothing for a metafilm with square period of 21 μm , square size of 15 μm , and SiO_2 layer thickness of 1.2 μm (black line). RLC circuit simulated with voltage equal to 1 V.	31
Figure 31.	Comparison of RLC circuit model performance against actual data for a metafilm with square period of 21 μm , varying square size, and SiO_2 layer thickness of 1.2 μm . Smooth curves are given by the RLC circuit model.	35
Figure 32.	As a function of square size, resistance necessary for RLC circuit to model experimental peak absorption data where 1 Ω corresponds to maximum absorption.....	40
Figure 33.	As a function of SiO_2 thickness, resistance necessary for RLC circuit to model experimental peak absorption data where 1 Ω corresponds to maximum absorption.	41
Figure 34.	1 / R as a function of 1 / Fill Factor fitted with a linear fit. Data points reaching near 100% absorption were not fitted since they obscure the linear relationship occurring below maximum absorption.	41
Figure 35.	1 / R as a function of SiO_2 thickness.....	42
Figure 36.	As a function of square size, inductance necessary for RLC circuit to model experimental FWHM data given the baseline resistance calculated in Table 5.	43

Figure 37.	Necessary inductance as a function of square area, fitted with a linear fit, excluding the last data point in the 1.6 μm thickness.....	44
Figure 38.	As a function of SiO_2 thickness, inductance necessary for RLC circuit to model experimental FWHM data given the baseline resistance calculated in Table 5.....	45
Figure 39.	As a function of square size, capacitance necessary for RLC circuit to model experimental resonant frequency data given the inductance calculated in Table 6.....	46
Figure 40.	Necessary capacitance as a function of square area, fitted with a linear fit, excluding the last data point in the 1.6 μm thickness.....	47
Figure 41.	As a function of SiO_2 thickness, capacitance necessary for RLC circuit to model experimental resonant frequency data given the inductance calculated in Table 6.....	47
Figure 42.	Raw data THz absorption of a metafilm with constant square period of 21 μm , varying square size, and SiO_2 layer thickness of 0.4 μm	51
Figure 43.	Raw data THz absorption of a metafilm with constant square period of 21 μm , varying square size, and SiO_2 layer thickness of 0.8 μm	51
Figure 44.	Raw data THz absorption of a metafilm with constant square period of 21 μm , varying square size, and SiO_2 layer thickness of 1.2 μm	52
Figure 45.	Raw data THz absorption of a metafilm with constant square period of 21 μm , varying square size, and SiO_2 layer thickness of 1.6 μm	52
Figure 46.	Raw data THz absorption of a metafilm with varying square period, constant square size of 16 μm , and SiO_2 layer thickness of 0.4 μm	53
Figure 47.	Raw data THz absorption of a metafilm with varying square period, constant square size of 16 μm , and SiO_2 layer thickness of 0.8 μm	53
Figure 48.	Raw data THz absorption of a metafilm with varying square period, constant square size of 16 μm , and SiO_2 layer thickness of 1.2 μm	54
Figure 49.	Raw data THz absorption of a metafilm with varying square period, constant square size of 16 μm , and SiO_2 layer thickness of 1.6 μm	54

THIS PAGE INTENTIONALLY LEFT BLANK

LIST OF TABLES

Table 1.	Comparison of resonant frequencies for SiO ₂ layer thickness of 1.2 μm with square period of 21 μm and varying square size.	33
Table 2.	Comparison of absorption peaks for SiO ₂ layer thickness of 0.8 μm with square period of 21 μm and varying square size.	37
Table 3.	Comparison of FWHM for SiO ₂ layer thickness of 0.8 μm with square period of 21 μm and varying square size.	38
Table 4.	Inductance required to support the parallel plate capacitance model compared to inductance required to support the RLC circuit model.	38
Table 5.	Resistance (Ω) necessary for RLC circuit to model experimental peak absorption data where 1 Ω corresponds to maximum absorption.	40
Table 6.	Inductance (pH) necessary for RLC circuit to model experimental FWHM data given the baseline resistance calculated in Table 5.	42
Table 7.	Capacitance (10^{-15} F) necessary for RLC circuit to model experimental resonant frequency data given the inductance calculated in Table 6.	45

THIS PAGE INTENTIONALLY LEFT BLANK

LIST OF ACRONYMS AND ABBREVIATIONS

THz	Terahertz
NPS	Naval Postgraduate School
SRL	Sensor Research Lab
NICT	National Institute of Information and Communications Technology
QCL	Quantum Cascade Laser
ISSTT	International Symposium on Space Terahertz Technology
MLS	Microwave Limb Sounder
MEMS	Microelectromechanical Systems
FTIR	Fourier Transform Infrared Spectrometer
FWHM	Full With Half Maximum
AC	Alternating Current

THIS PAGE INTENTIONALLY LEFT BLANK

ACKNOWLEDGMENTS

It was truly a blessing to be a part of the research taking place in Dr. Karunasiri's lab. Those working there are excited about what they are doing, eager to share their knowledge and experience, and quick to lend a helping hand whenever needed. Enough thanks cannot go out to Dr. Karunasiri, Dr. Alves, and Brian Kearney. Their insight and guidance were vital to the success of this research. Additional thanks to Dr. Grbovic and Dr. Newman for their contributions in bettering this research. Their genuine concern for making this a worthwhile endeavor is much appreciated.

THIS PAGE INTENTIONALLY LEFT BLANK

I. INTRODUCTION

A. METAMATERIAL ABSORBERS

Metamaterials are subwavelength composites that exhibit properties not found in nature, such as a negative refractive index [1]. While negative electrical permittivity (ϵ) and negative magnetic permeability (μ), though less common, are both found in natural materials, they are not found simultaneously within the same frequency band [1]. Metamaterials are able to achieve both a negative ϵ and a negative μ simultaneously and thus a negative refractive index. The ability to tune the electrical permittivity and magnetic permeability by controlling constituents, materials, and configurations is a distinct advantage of metamaterials. This leads to unique and interesting applications such as cloaking [2], earthquake resistant structures [2], and terahertz (THz) technologies [3], as well as improvements to existing technologies such as antenna design and performance [2].

Of interest for this research is the absorption capability of metamaterials in the THz region which spans the electromagnetic spectrum from 100 GHz to 10 THz where $1 \text{ THz} = 10^{12} \text{ Hz}$. This region is also considered the far-IR and lies in between the microwave and infrared wavelengths. There are many capable and efficient devices that operate in the microwave and visible/infrared wavelengths, however, due to the inefficiency of electronic and photonic responses in the THz region, it is “arguably the least developed and least understood portion of the EM spectrum scientifically and technologically” [1].

The Naval Postgraduate School (NPS) Sensor Research Lab (SRL) is working on the optimization and design of metamaterial absorbers in the THz region. Through this research, metamaterial absorbers have been developed that demonstrate near 100 percent absorption [3]. These absorbers are generally comprised of a metallic ground plane separated from a periodic array of metal cells by a dielectric layer as shown in Figure 1. Such an array comprises a thin film of metamaterial, also referred to as a metafilm [2].

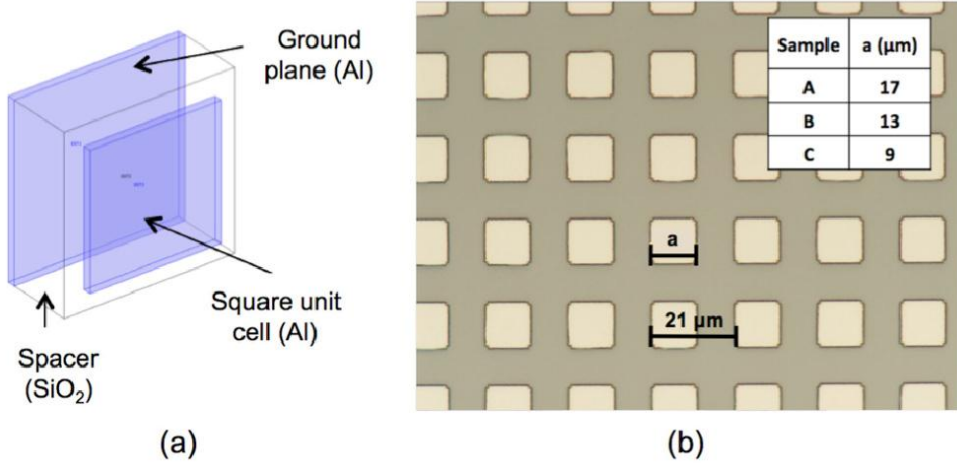


Figure 1. Metamaterial cell (a) and periodic array of cells (b) from [4].

There are differing views as to how exactly these metamaterial absorbers operate. The main argument is that the metamaterial effectively matches impedance with the surrounding material, or air in most cases, thus minimizing reflection [3]. These materials are designed so that there is no transmission. Therefore, if reflection is completely eliminated, 100 percent absorption is achieved [3]. Some contend more specifically that the effective impedance matching is due to the Fabry-Perot effect [5]. Regardless of the model used to explain the phenomenon, studies have clearly witnessed an effective impedance matching which allows for metamaterial absorption [4].

B. USES OF TERAHERTZ TECHNOLOGY

Over the past decade, there has been increasing interest in the THz region and its applications. In April 2006, the National Institute of Information and Communications Technology (NICT) in Japan began the Terahertz Project, intending to shape Japanese infrastructure in support of THz applications [6]. The THz wavelength is short enough to allow sub-millimeter resolution while also long enough to allow penetration of most nonmetals [7]. Additionally, the unique absorption characteristics of many materials in the THz region allows for spectroscopic “fingerprints” to be cataloged. With an established database of known spectra for targeted materials, THz devices can be used to

identify these materials when other means of identification are difficult or unachievable [6]. These characteristics lead to some interesting applications in both the security and medical fields.

With its object penetrating capability, real time THz imaging provides wide-sweeping applications in security, including detection of concealed weapons, explosives, narcotics, and buried mines. Utilizing fingerprinting, explosives and narcotics are detectable and identifiable by their unique spectra in the THz region [8]. Additionally, THz based devices are capable of greater resolution than current microwave based airport security screening equipment due to the shorter wavelength.

Uses in the medical field are also vast and constantly under further exploration. The THz wavelength is non-ionizing and sensitive to the motions of molecules [9]. This allows for observations that are unachievable in other wavelengths such as the infrared where objects sometimes change form under heat treatment [8]. THz technology has demonstrated the capability to detect cancer [7], determine varying degrees of burns [10], and even discern between single and double stranded DNA [9].

While there are many other areas of interest involving the THz wavelength, there are those who are not as optimistic about the applications of THz technology [11]. The two main reasons for this outlook are the atmospheric absorption challenge of THz energy along with the challenge of creating devices which efficiently produce THz energy. THz radiation faces severe absorption challenges through the atmosphere, attenuating as much as 100,000 decibels/km at 5 THz versus only 0.2 decibels/km at 50 GHz [11]. This does not negate the potential uses of THz technologies, although it does mitigate their effectiveness in some applications. For instance, a terrestrial wide-band communication link operating at 1 THz would have great difficulty at distances greater than 100 meters [11]. Others argue that this could be an advantage for short range communications in the tactical environment, allowing the enemy less opportunity to intercept or jam [12].

Because THz radiation is rapidly absorbed by the atmosphere, an illuminating source is necessary for most applications, which provides the other challenge. There is

heavy research and development in THz sources, but efficiencies of such sources remain below one percent [11]. Again, this may limit the extent of applications in the THz region; however, current THz sources are adequate for a number of applications, such as real time imaging under development at NPS SRL with the use of a quantum cascade laser (QCL). Additionally, due to these challenges, space may provide the ideal environment for operation at THz frequencies.

C. APPLICATIONS OF TERAHERTZ TECHNOLOGY IN SPACE

Due to the challenges of atmospheric absorption and THz source efficiency, space is an outstanding environment for THz application. Not only are the atmospheric losses eliminated in space, there is also an abundance of THz energy sources. A statistic given by astronomer David Leisawitz at NASA Goddard Space Flight Center is “that 98 percent of the photons released since the big bang reside in the submillimeter and far-infrared bands” [11]. Bearing in mind that THz is equivalent to far-infrared, this means that there is a lot of energy available for observation in the THz region. As Peter Siegel at Cal Tech states “the universe is bathed in terahertz energy; most of it going unnoticed and undetected” [13]. THz spectrometers have been used as far back as the 1970s for observing and characterizing interstellar medium as well as the atmospheric composition of planets [11]. The interest in astrophysical observations led NASA to establish the International Symposium on Space Terahertz Technology (ISSTT) in 1990 [14]. With regard to current and future applications of THz technology in space, the most interest lies in the continued study of astrophysical observations and planetary atmospheric observations within the solar system.

Space based THz detection systems for astronomy were being developed as early as 1990 and have been undergoing continual improvement ever since [14]. The observations and spectral analyses provided by such collection garner tremendous insight for modern cosmology as well as for star formation and galactic structure [15]. For example, galactic redshift is strong in the THz region [13], and exploration there has led to the discovery of thousands of galaxies undetected in the visible or infrared [16]. Another example of the importance of observations in the THz region involves

interstellar clouds. Interstellar clouds are believed to be instrumental in the life cycle of galaxies and to be fundamental in the formation of stars and planets; however, very little is understood about their formation [16]. Due to the cold physical conditions within the clouds, there is little opportunity for observation outside of the THz realm [16]. Recent observations conducted in the THz region by Herschel are helping to generate theories as to how these clouds form [16]. Herschel, launched in May of 2009, is a far-infrared space telescope operating between 0.5 to 1.9 THz.

While Herschel is pursuing the study of astrophysics within the Milky Way as well as the galaxies beyond, another interest for THz lies in the study of Earth's atmosphere and other planetary atmospheres within the solar system. By observing atmospheres in the THz region, much insight can be gained in understanding the physical and chemical processes occurring [16]. With regard to Earth, such observations assist in ozone destruction monitoring, global warming analysis, total radiation balance analysis, and pollution monitoring [13]. Launched in July of 2004, the Aura spacecraft, for example, provides observations of the Earth's atmosphere with the mission of globally mapping OH. Using a 2.5 THz CO₂ pumped methanol gas laser, the microwave limb sounder (MLS) onboard Aura illuminates gases in the atmosphere so that their THz spectral characteristics can then be observed [17]. A similar capability is desired for other missions as well. The Outer Planets Flagship Missions to Saturn and Jupiter desire to incorporate a THz instrument onboard for atmospheric analysis [18].

D. DISCUSSION OF RESEARCH

To improve the state-of-the-art THz sensing, the SRL is researching the design and fabrication of THz optimized bi-material microelectromechanical systems (MEMS) arrays for THz imaging, shown in Figure 2(a) along with the structure of one pixel (Figure 2(b)). The simulated operation of a similar pixel is shown in Figure 3.

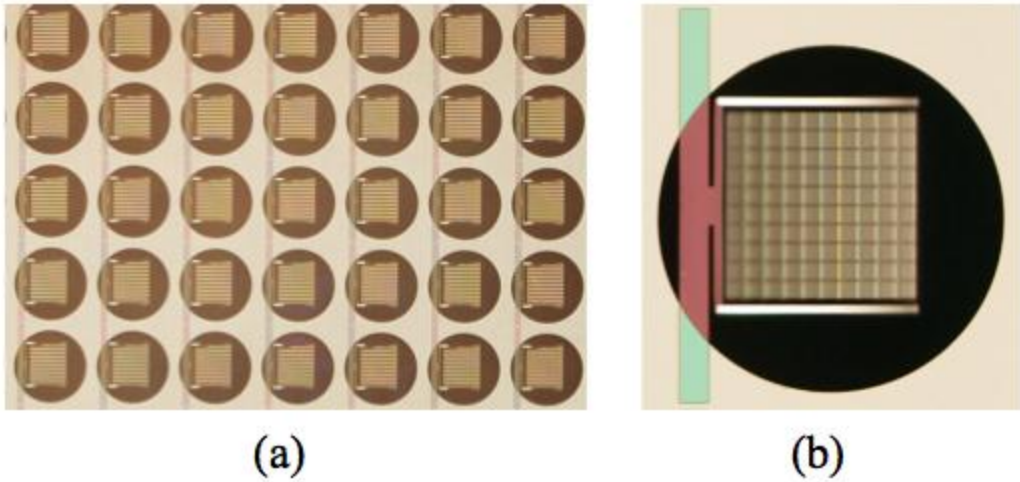


Figure 2. Micrograph of the metamaterial-based THz bi-material sensor array under development in the Sensor Research Lab at the Naval Postgraduate School.
 (a) Partial view of the array; (b) zoom of a single pixel.

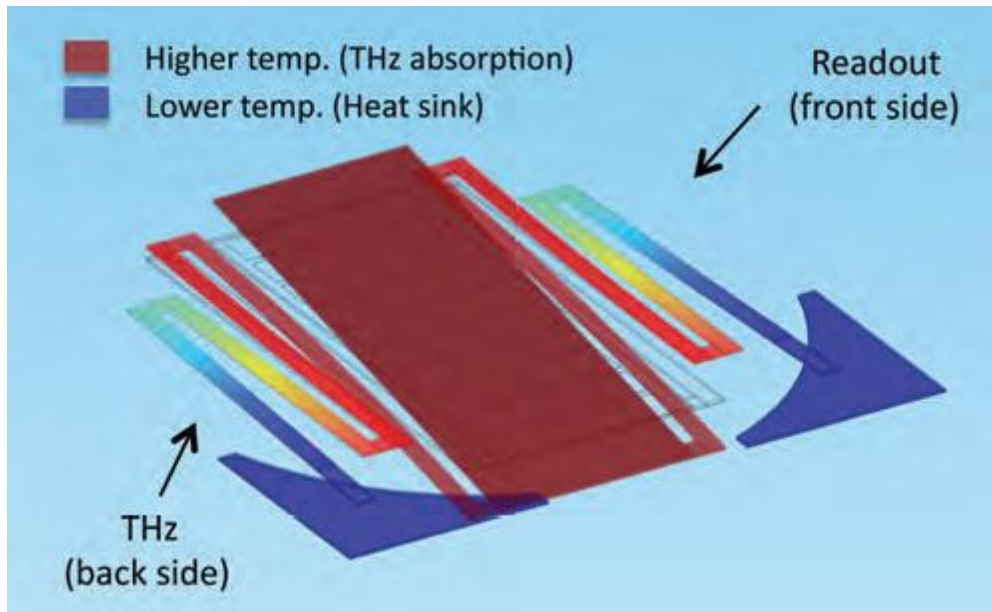


Figure 3. COMSOL analysis of bi-material sensor with THz metafilm from [2].

Crucial to the development of one of these pixels is the metamaterial absorption layer (metafilm from section 1-A) sensitive to THz (Figure 1). When THz radiation is absorbed by the metafilm lying at the center of the pixel, it heats up, creating a temperature difference across the structure. This temperature difference causes the structure to bend as shown in Figure 3. By measuring the amount of deflection in the

structure with optical readouts, the intensity of the THz radiation can be determined and thus displayed as an image given an array of pixels [19].

This thesis seeks to gain better understanding of the absorption characteristics of the metafilms necessary for these bi-material structures—specifically how dielectric thickness and metamaterial dimensions affect absorption percentage and frequency. In order to allow for this study, the SRL fabricated ten wafers, each containing 25 different metamaterial configurations for a total of 250 configurations. Each wafer consists of a 95 nm thick Al ground plane with an SiO_2 dielectric spacing it from a 95 mm thick aluminum square patch as shown in Figure 1. The SiO_2 layer varies from 0.4 to 2.0 μm , depending on the wafer. The patterns within each wafer are then of consistent dielectric thickness but varying square patch size, periodicity, and pattern. An example of one of these wafers is shown in Figure 4.



Figure 4. Wafer with 25 different metamaterial configurations.

The scope of this research includes collecting data on each wafer, analyzing that data, and creating equivalent electrostatic models [4] whose performance matches the data.

E. BENEFITS OF RESEARCH

While current studies are already being conducted in the THz region, improvements in sensor technology are still needed. This research directly contributes to the design and fabrication of THz metamaterial sensors which are both more sensitive and less expensive than their current counterparts, while allowing real time imaging. The higher sensitivity is achieved through the capability of near 100 percent absorption, while the reductions in cost are achieved through less expensive fabrication techniques along with the lack of operational cooling requirements. In addition to these advantages is the expectation that these sensors will be lighter than their contemporaries. All of these are advantageous to the space community. Specifically, advancements in astronomy call for more sensitive sensors, especially above 1.6 THz [16], and this research targets frequencies between 1–10 THz. Given the advantages of THz metamaterial sensors along with the interest in THz sensors onboard spacecraft, it seems very likely that metamaterial based sensors will one day be a reality in space.

With regard to how this research specifically contributes to the advancement of THz metamaterial sensors, it provides insight on how to optimize and efficiently design the sensors for a target frequency with maximum absorption. The aim is that this understanding will contribute to the design process, making it simpler, more effective, and less costly. This should ultimately lead to the establishment of a standard method for designing and fabricating THz metamaterials to meet desired performance.

The immediate benefit of this research should be seen in the SRL's design of a THz imaging device. As discussed in section 1-D, the metafilm is an essential component of the bi-material structure being used for the design of a THz imaging device.

II. DATA COLLECTION & ANALYSIS

A. DATA COLLECTION PROCESS & METHODS USED

As previously discussed in section 1-D, ten wafers were fabricated with 25 different structures on each for data collection. Each wafer was characterized using a Fourier transform infrared spectrometer (FTIR) Nexus 8700 fitted with a globar beam source, Si beam splitter, and a pyroelectric detector. Using the FTIR, reflection (R) and transmission (T) are measured over the range of THz frequencies, and absorption (A) percentage is obtained using $A = 100 - R - T$.

1. Operation of the FTIR

The FTIR allows a broadband light source to achieve what would otherwise require over a thousand monochromatic measurements at differing frequencies. By using a Michelson interferometer, where one of the mirrors moves to vary the phase difference between the two light paths, the FTIR measures how intensity varies as path distance (Δy) varies. A general schematic for the FTIR is shown in Figure 5.

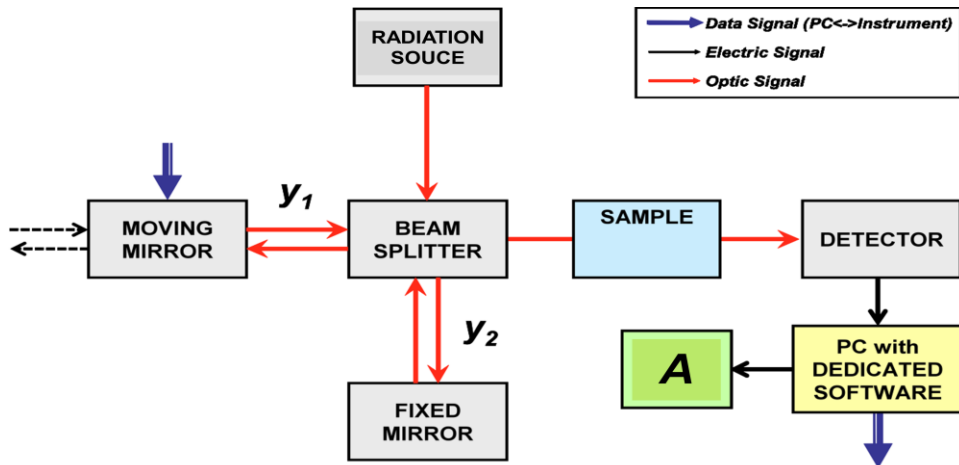


Figure 5. Schematic diagram of a Fourier Transform Infrared Spectrometer.

The intensity (I) of the light received by the detector as a function of path distance (Δy) is given by the following equation (where σ is the wavenumber):

$$I(\Delta y) = \int_0^{\infty} I(\Delta y, \sigma) d\sigma = \int_0^{\infty} \frac{E_0^2(\sigma)}{2} d\sigma + \int_0^{\infty} \frac{E_0^2(\sigma)}{2} \cos(2\pi\sigma\Delta y) d\sigma \quad (2.1)$$

By taking the Fourier transform of the second term in Equation 2.1, called the interferogram, the absorption data is mapped for a given frequency interval. In this way the FTIR is able to extract frequency specific absorption data with a broadband infrared source. This is possible because the phase difference between the two light paths is wavelength dependent. The moving mirror allows data collection of this dependence, while the Fourier transform of that data reveals the absorption for each individual frequency.

2. Setup of the FTIR

The FTIR accessory attachment, MappIR, allows two configurations for data collection as shown in Figure 6.

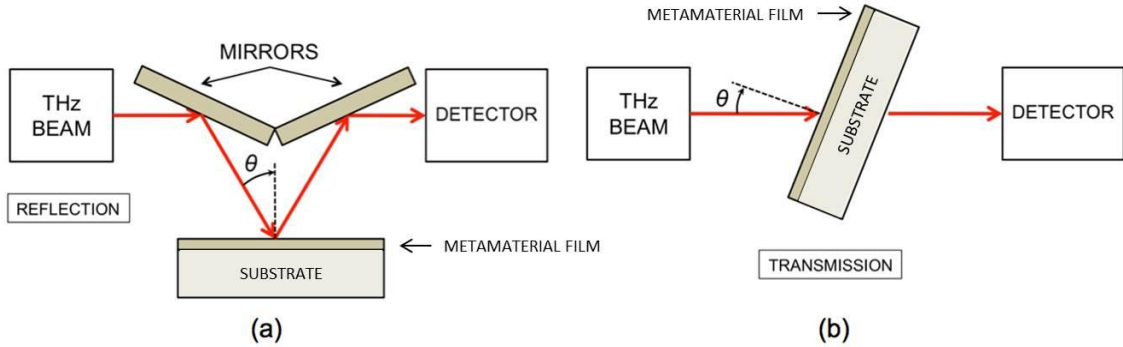


Figure 6. Schematic of the experimental configuration used for measuring the reflection (a) and transmission (b). The incidence angle (θ) is 15° for both configurations.

Configuration (a) allows the measurement of reflected THz energy off of the wafer. Configuration (b) allows the measurement of transmittance. Since the metamaterial films were designed to block transmission in the THz range, the

configuration shown in Figure 6(b) allows verification of this property. Once it is verified that the wafer does not allow transmittance, reflection measurements are utilized for all data collection, and absorption percentage is obtained by $A = 100 - R$.

First, the background is measured by placing a gold mirror in the MappIR tray. This establishes the amount of energy that the sensor expects in the case of 100 percent reflection, as the gold mirror is nearly a perfect reflector in the THz range. All following measurements are compared to this amount to obtain reflection percentage. Following the background measurement, the wafer to be characterized is placed in the tray. Within four hours, MappIR positions all 25 sectors on a wafer through the FTIR for characterization.

It was verified for all ten wafers that zero transmittance was allowed through the Al ground plane. Additionally, a new background was established prior to data collection on each wafer. Since THz energy is highly absorbed by H_2O in the air, the FTIR was under constant purge with dry air to prevent erroneous data due to absorption by moisture in the laboratory air.

3. Parameters for Data Collection

Two programs were utilized in coordination with the FTIR to establish the operating parameters for data collection—OMNIC & AutoPRO. The general setup used for each is shown in Figures 7 and 8.

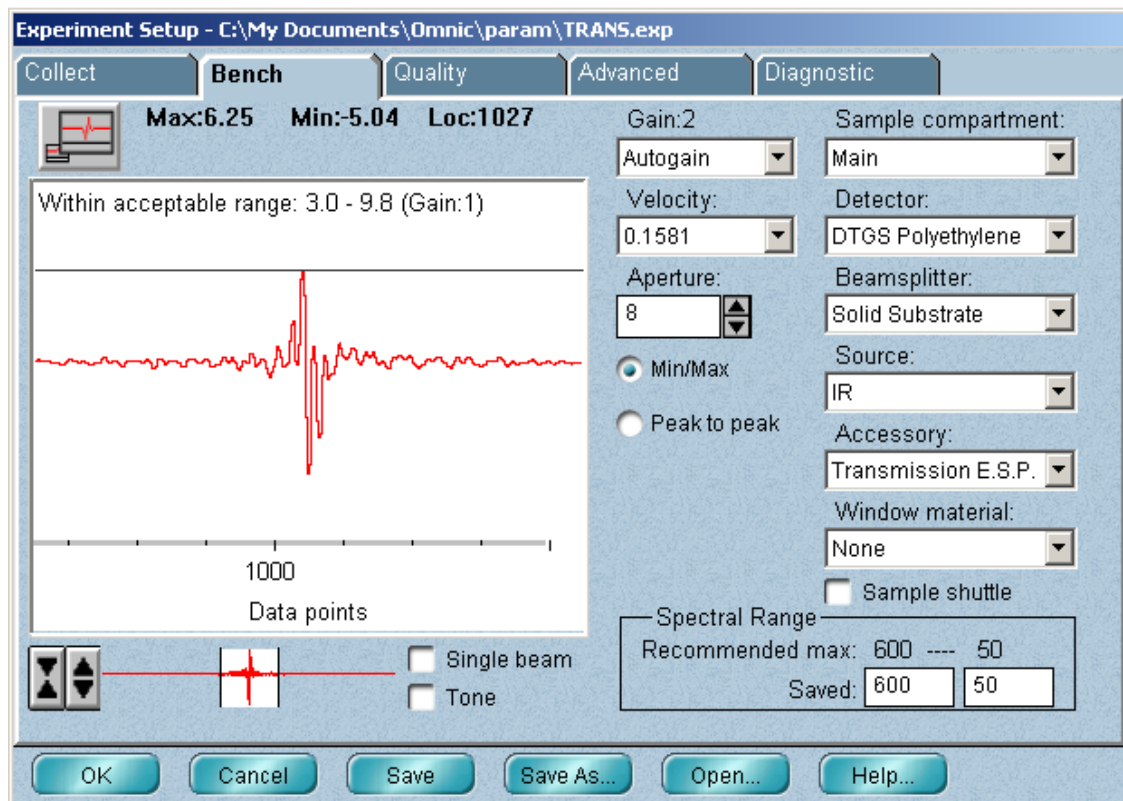


Figure 7. Experimental bench setup in OMNIC displaying key parameters for data collection.

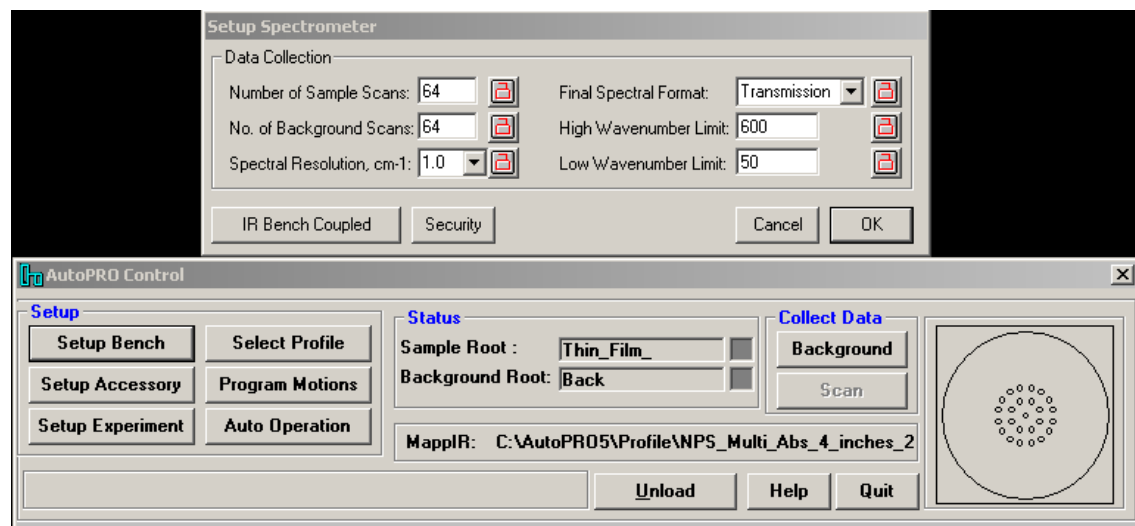


Figure 8. Experimental setup in AutoPRO displaying key parameters for data collection.

Key parameters to note are the spectral range, spectral resolution, and mirror velocity. With regard to spectral range, data was collected over the range of 50 to 600

wavenumbers, or 1.5 to 18 THz. With regard to spectral resolution, maximum resolution was desired for accuracy and clarity. Figure 8 shows that 1.0 cm^{-1} was configured, as this is the maximum allowable by the system; however, this actually correlated to a spectral resolution of approximately 0.5 cm^{-1} in the data. The velocity parameter, shown in Figure 7, correlates to the speed (cm/s) of the moving mirror in the interferometer. A slower velocity is desired for less noisy measurements. Also of note is the scan pattern showing the 25 different sectors of the wafer for independent analysis, seen at the bottom right of Figure 8.

B. PRESENTATION OF DATA COLLECTED & ANALYSIS

While data was collected, plotted, and observed for ten different wafers, only data for four of the wafers is presented with analysis. This emphasizes the best of the data collected and the contrast between varying dielectric thicknesses. SiO_2 thicknesses of 0.4, 0.8, 1.2, and 1.6 μm are presented. Additionally, this study focuses on sectors 1–16 of these wafers which involves varying square size and varying period. Figure 1(b) displays square size, labeled “a,” and period, labeled “21 μm .”

1. Varying Square Size

Sectors 1–10 on each wafer hold square period fixed at 21 μm while varying square size from 18 μm down to 9 μm . The smoothed raw data, presented in Figures 9, 10, 11, and 12, reveals that there is a clear correlation between square size and the THz frequency of peak absorption as well as magnitude of absorption. Additionally, there is a clear increase in THz absorption as the SiO_2 thickness increases. Figure 9 highlights the complete absorption curve between 3.5 and 9 THz, while Figures 10, 11 and 12 show the curve above 20 percent absorption for clarity of illustration. Savitzky-Golay smoothing was used, and the raw data, unsmoothed, can be found in Appendix A. There it can be seen that only limited smoothing was necessary and that the greatest margin error lies with the 0.4 μm SiO_2 thickness, where the data is noisier than for the other dielectric thicknesses.

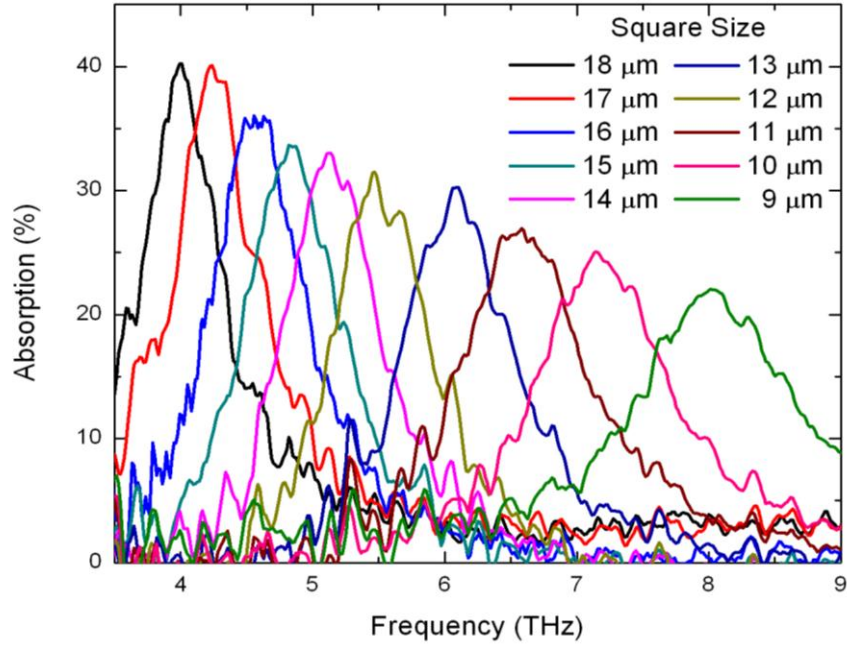


Figure 9. THz absorption of a metafilm with constant square period of $21 \mu\text{m}$, varying square size, and SiO_2 layer thickness of $0.4 \mu\text{m}$.

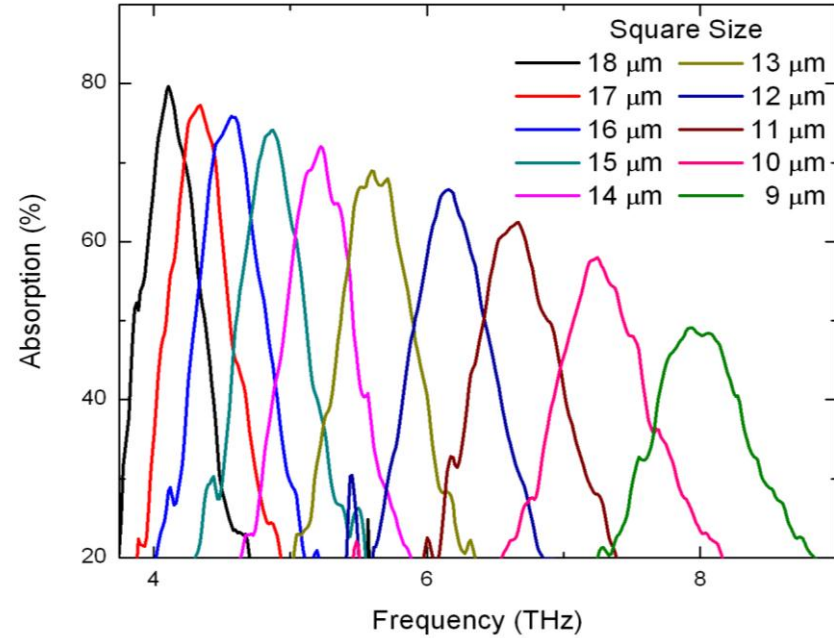


Figure 10. THz absorption of a metafilm with constant square period of $21 \mu\text{m}$, varying square size, and SiO_2 layer thickness of $0.8 \mu\text{m}$.

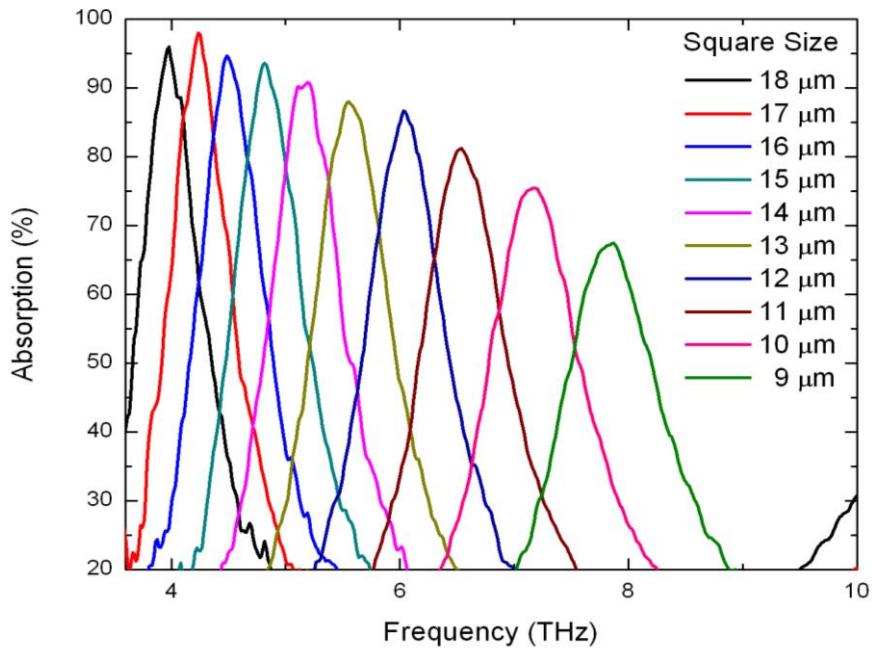


Figure 11. THz absorption of a metafilm with constant square period of $21 \mu\text{m}$, varying square size, and SiO_2 layer thickness of $1.2 \mu\text{m}$.

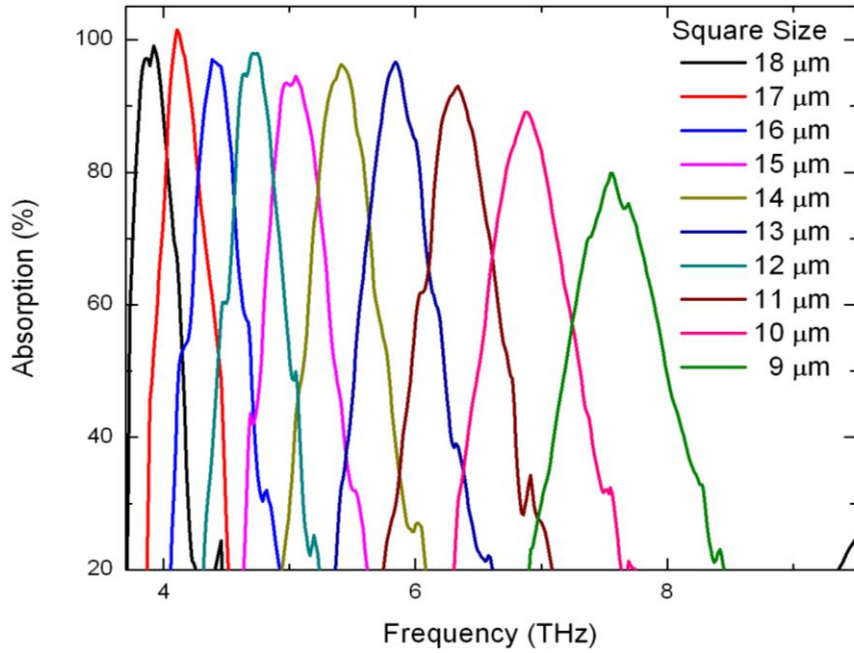


Figure 12. THz absorption of a metafilm with constant square period of $21 \mu\text{m}$, varying square size, and SiO_2 layer thickness of $1.6 \mu\text{m}$.

In addition to observing an increase in absorption as SiO_2 thickness increases, it is also observed that a decrease in square size generally leads to a decrease in absorption magnitude. This is expected since the effective area of absorption is reduced when square size is reduced while square period is kept constant. The absorption peaks are plotted against SiO_2 thickness in Figure 13 to further illustrate these trends.

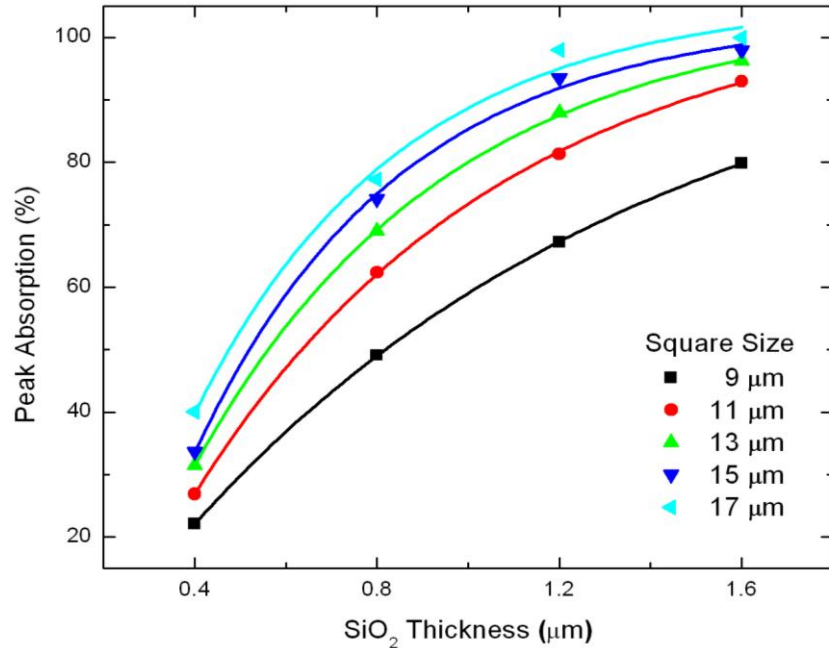


Figure 13. Peak absorption increases as SiO_2 thickness increases for varying square size with constant square period of 21 μm . Data points are fitted with an exponential fit for clarity of trend using the equation $y = y_0 + Ae^{R_0x}$.

The effect of increasing absorption with increasing SiO_2 thickness is observed to taper off exponentially for the given metafilms. This indicates that there is an optimal thickness depending on the square size. It also shows that some square sizes may be unable to achieve 100 percent absorption, regardless of thickness. While the data appears to fit exponentially, this may be misleading since there are so few data points. The phenomena may be better explained by another mathematical relationship. The rapid decrease in absorption as SiO_2 thickness decreases is believed to be due to greater impedance mismatch between the metafilm and air, causing greater reflection [3].

Figures 9, 10, 11 and 12 also revealed a shift in frequency for the absorption curves as square size was reduced. This is better illustrated in Figure 14 where the slight frequency shift based upon SiO_2 thickness can also be observed.

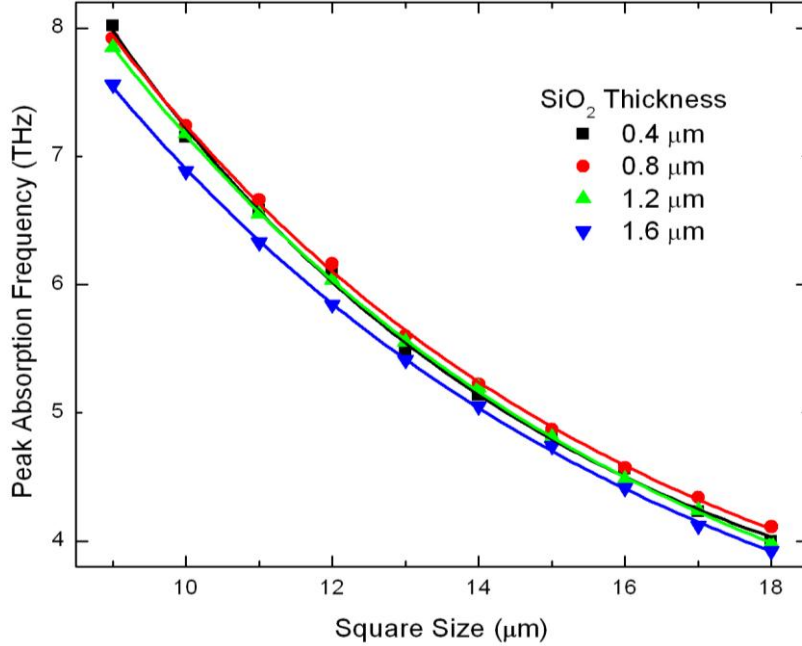


Figure 14. Peak absorption frequency shifts as a function of square size with constant square period of 21 μm . Data points are fitted with an exponential fit for better observation of trending behavior using equation $y = y_0 + Ae^{R_0x}$.

The data in Figure 14 fits well to the exponential function $y = y_0 + Ae^{R_0x}$; however, further analysis reveals that there is a linear relationship between peak absorption frequency and inverse square size. This relationship correlates well with the notion of an RLC circuit model where resonant frequency $= 1/\sqrt{LC}$ and capacitance (C) exhibits a direct dependence on square area (A) given by the parallel plate equation $C = \epsilon A/d$ (where ϵ is the dielectric constant and d is the distance between the two metal plates) [4]. This result is shown in Figure 15.

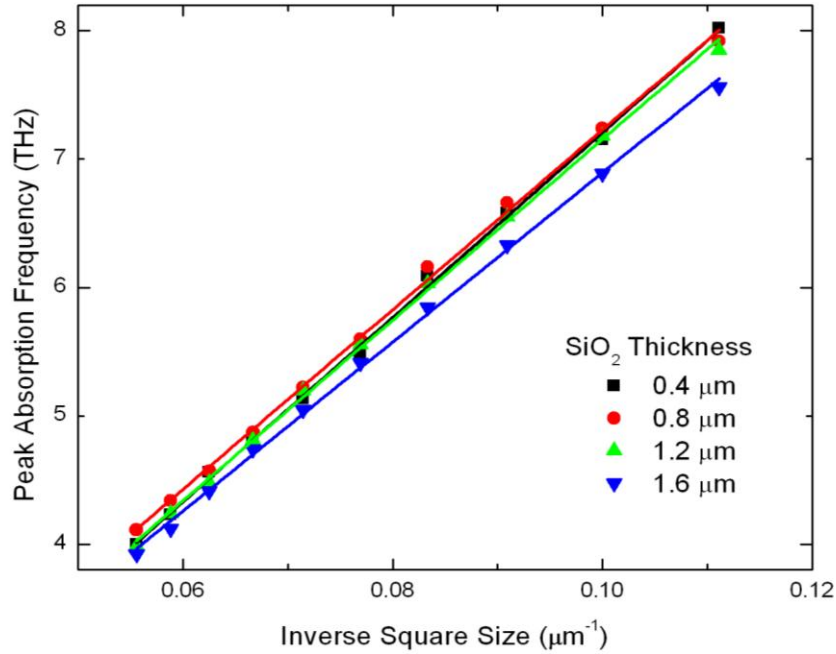


Figure 15. Peak absorption frequency shifts as a function of inverse square size with constant square period of 21 μm . Data points are fitted with a linear fit.

Similar behavior, though not as distinct, is observed with the full width half maximum (FWHM) plots. Figure 16 demonstrates an exponential fit of the data using equation $y = y_0 + Ae^{R_0x}$, while Figure 17 demonstrates linearization of the data, using inverse square size vice square size. The fluctuations among the 0.4 μm thickness are most likely due to the error in that data. As previously mentioned and shown in Appendix A, the absorption data for the 0.4 μm thickness is not as clear as for the other thicknesses. This should be kept in mind throughout the analysis.

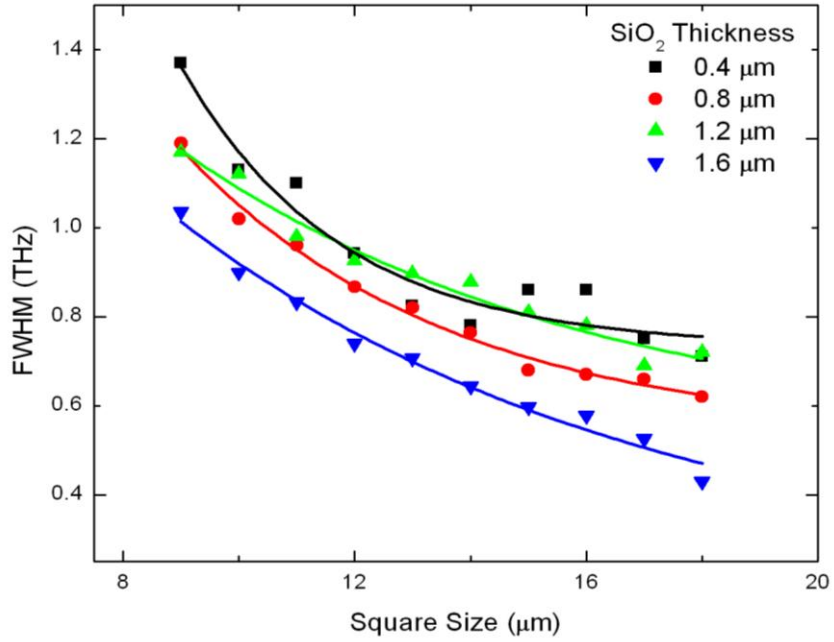


Figure 16. Full width half maximum (FWHM) shifts as a function of square size with constant square period of 21 μm . Data points are fitted with an exponential fit for better observation of trending behavior using equation $y = y_0 + Ae^{R_0x}$.

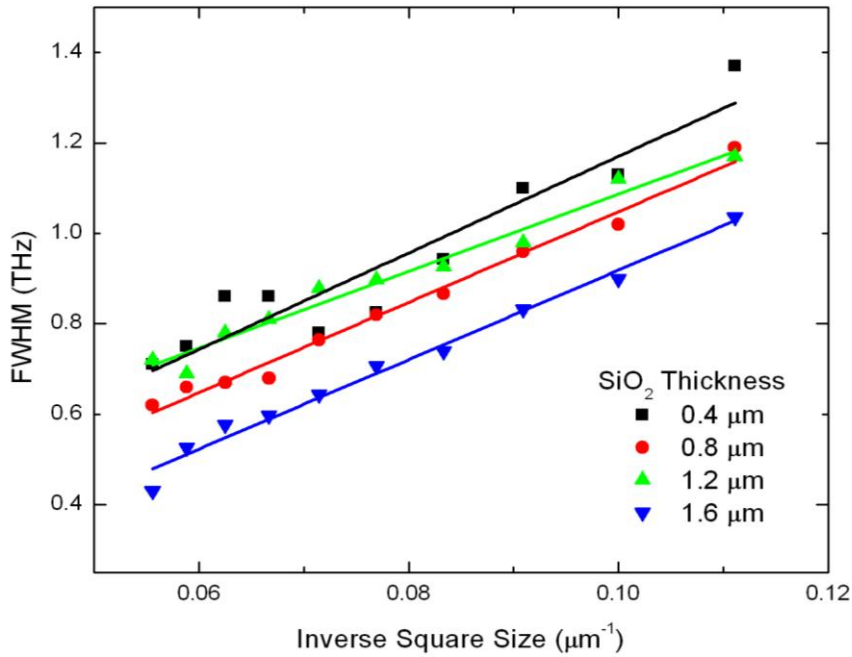


Figure 17. Full width half maximum (FWHM) shifts as a function of inverse square size with constant square period of 21 μm . Data points are fitted with a linear fit.

The obvious trend shown in Figure 16 is that square size directly affects the width of the absorption spectrum, with a smaller square size correlating to a larger width. Since a smaller square size correlates to lower peak absorption, there is a distinct tradeoff between high absorption and broad bandwidth. In order to understand how the FWHMs compare relative to their resonant frequency or center frequency (previously referred to as the peak absorption frequency), the quality factor was also plotted against square size as shown in Figure 18.

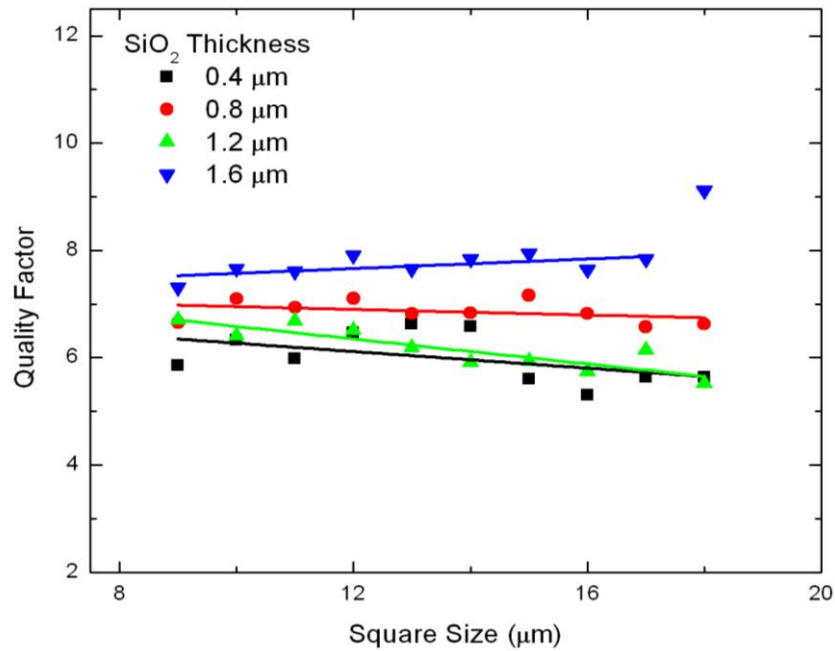


Figure 18. Quality Factor, defined as resonant frequency divided by FWHM, as a function of square size with constant square period of 21 μm . Data points are fitted with a linear fit. In the case of the 1.6 μm SiO_2 , the last data point is ignored.

While Figure 18 does not demonstrate a clear effect of square size upon quality factor (i.e., quality factor is almost constant), it does show that quality factor is slightly affected by SiO_2 thickness. The thickest SiO_2 layer maintains the highest quality factor with a maximum increase of as much as 2.5 over the other thicknesses. With the exception of the data inversion between 0.8 μm and 1.2 μm , an increase in SiO_2 thickness causes an increase in quality factor. This inversion may be due to over-etching in the

fabrication of the wafer, and further analysis is needed to confirm it. When creating the aluminum square pattern on the top of the metafilm, there is the potential to “over-etch” and thus create grooves between the metallic squares in the SiO_2 layer below. Since a change in the dielectric layer affects the index of refraction (η) of the metafilm, over-etch has the potential to shift the frequency of absorption. For larger square sizes this effect is smaller since there is less space between the squares.

The final comparison of interest with regard to varying square size is the effect of fill factor on peak absorption where fill factor is defined as square size squared (square area) divided by square period squared. Fill factor vs. peak absorption is shown in Figure 19.

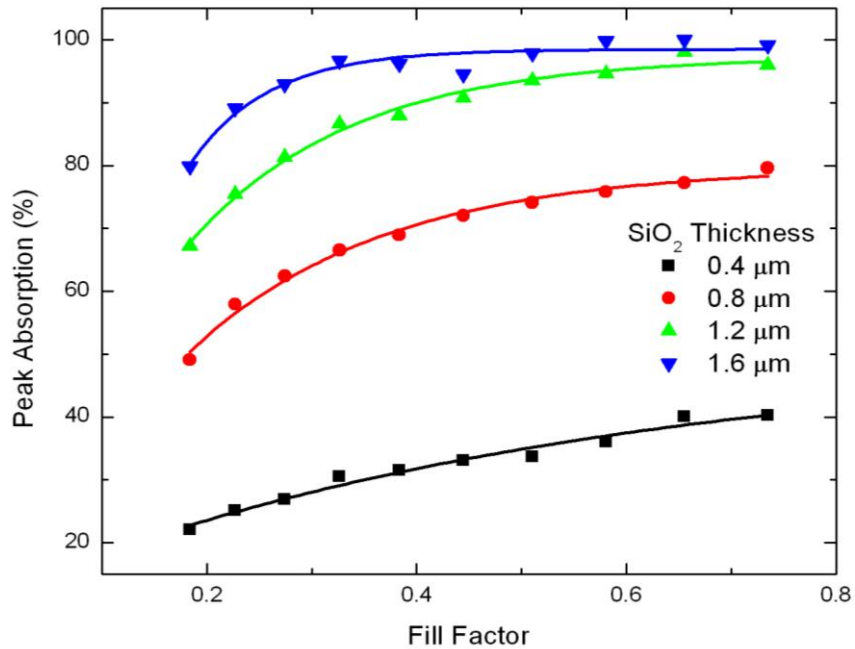


Figure 19. Peak absorption as a function of fill factor where square period remains constant at 21 μm . Data points are fitted with an exponential fit for clarity of trend using equation $y = y_0 + Ae^{R_0x}$.

As the square size increases, fill factor increases. As previously discussed, an increase in square size results in an increase in absorption, so as expected, an increase in fill factor correlates to an increase in absorption. It is interesting to note that as the SiO_2

thickness increases, the knee of the curve shifts to the left, meaning a thicker dielectric can utilize a smaller fill factor without significant absorption loss. Along the same lines, fill factor shows minimal effect on absorption for the thicker dielectrics once the knee of the curve is passed. The knee is very broad in the case of the thinner dielectrics, and so fill factor has a greater effect.

Interestingly, the peak absorption plotted against inverse fill factor reveals a linear relationship between the two as shown in Figure 20. This is especially true of the 0.4 and 0.8 μm thicknesses, while the 1.6 μm thickness does not fit as well due to the larger square sizes achieving near maximum absorption. Since absorption cannot rise above 100 percent, the data must plateau making it impossible for a linear fit when maximum absorption has been reached. There is, then, a region over which absorption relates linearly to inverse fill factor.

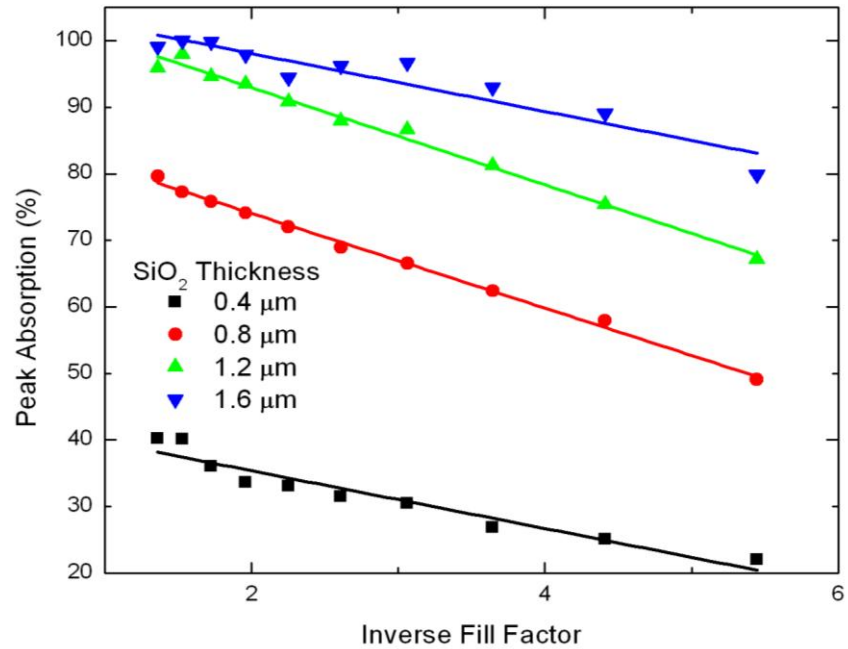


Figure 20. Peak absorption as a function of inverse fill factor where square period remains constant at 21 μm . Data fitted with a linear fit.

2. Varying Square Period

Sectors 11–16 on each wafer hold square size fixed at 16 μm while varying square period from 19 μm to 25 μm skipping period of 21 μm since that configuration is identical to sector 3. The smoothed raw data, presented in Figures 21, 22, 23 and 24, reveals that there is a clear correlation between square period and the percentage of THz absorption and very little correlation with regard to frequency of peak absorption. Additionally, as also observed in sectors 1–10, there is a clear increase in THz absorption as the SiO_2 thickness increases. Savitzky-Golay smoothing was used, and the raw data, unsmoothed, can be found in Appendix A. There it can be seen that only limited smoothing was necessary and that the greatest error lies with the 0.4 μm SiO_2 thickness, where the data is noisier than for the other dielectric thicknesses.

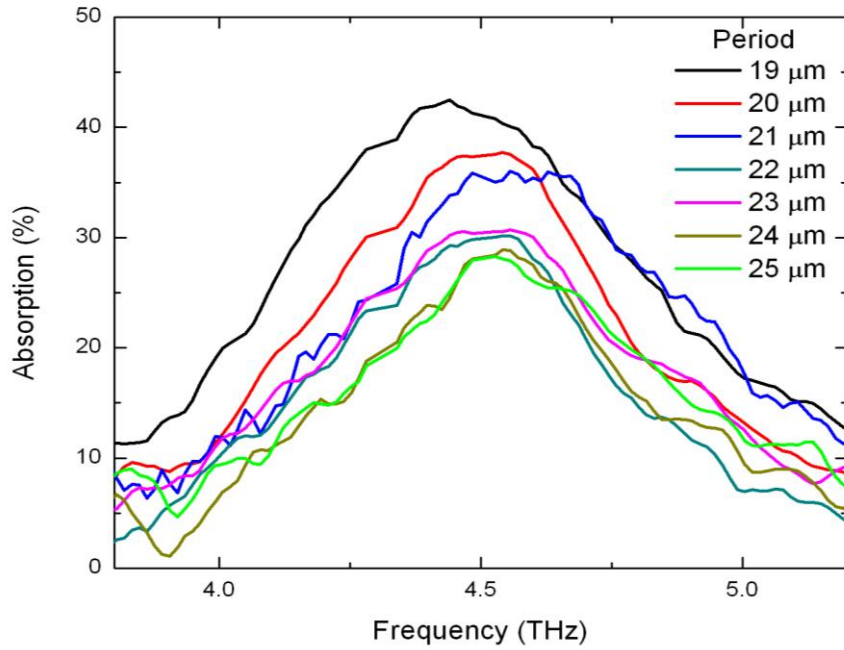


Figure 21. THz absorption of a metafilm with varying square period, constant square size of 16 μm , and SiO_2 layer thickness of 0.4 μm .

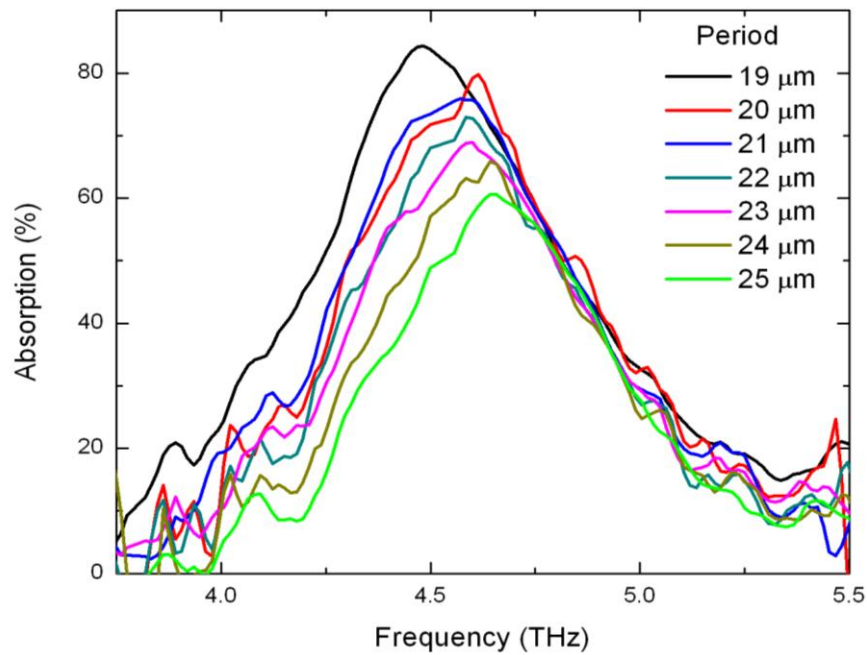


Figure 22. THz absorption of a metafilm with varying square period, constant square size of 16 μm , and SiO_2 layer thickness of 0.8 μm .

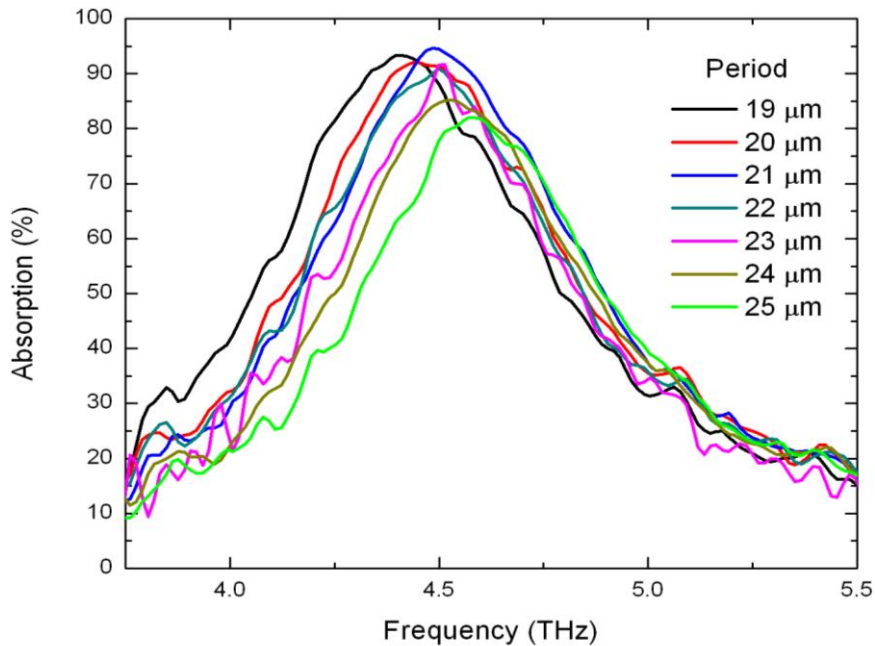


Figure 23. THz absorption of a metafilm with varying square period, constant square size of 16 μm , and SiO_2 layer thickness of 1.2 μm .

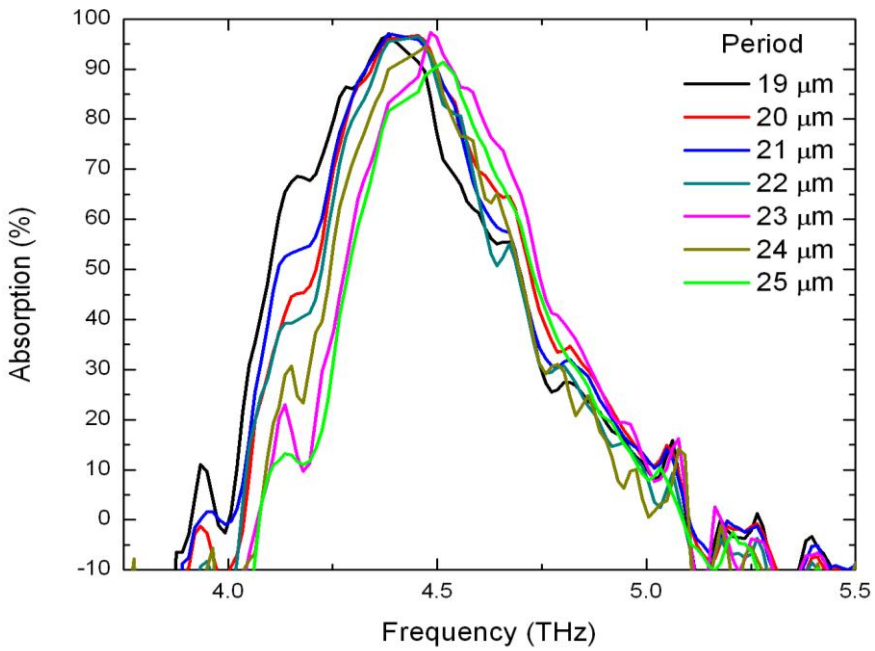


Figure 24. THz absorption of a metafilm with varying square period, constant square size of 16 μm , and SiO_2 layer thickness of 1.6 μm .

A decrease in square period generally leads to an increase in peak absorption. This is expected since fill factor increases when square period is reduced. The absorption peaks are plotted against SiO_2 thickness in Figure 25 to further illustrate this trend.

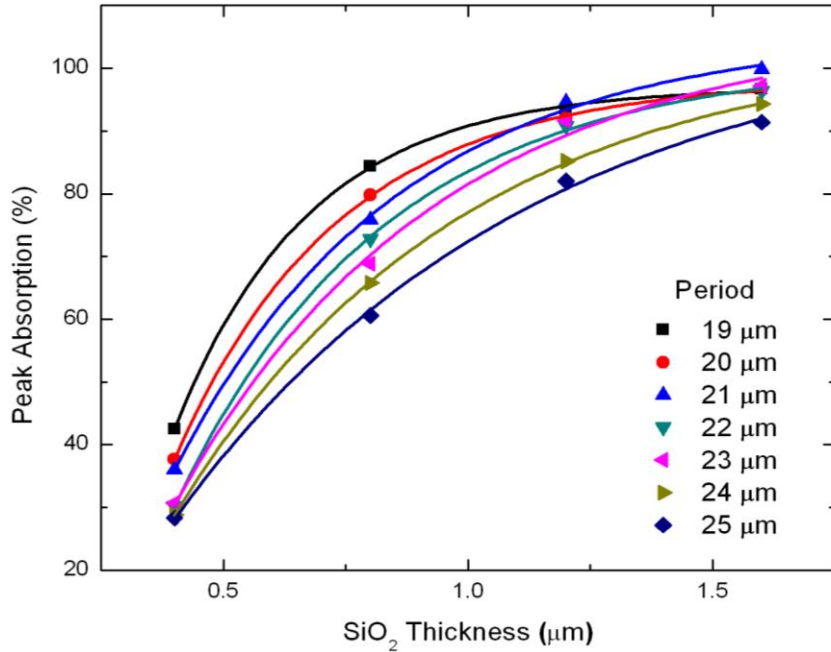


Figure 25. Peak absorption increases as SiO_2 thickness increases for varying square period with constant square size of 16 μm . Data points are fitted with an exponential fit for clarity of trend using equation $y = y_0 + Ae^{R_0x}$.

Figure 25 is in agreement with Figure 13, showing that an increase in SiO_2 thickness results in a consistent response, regardless of square size or square period. Interestingly, the absorption of metafilms with square periods 19 μm and 20 μm level out more quickly and are surpassed by a few of the larger periods.

When peak absorption is plotted against square period for the various SiO_2 thicknesses, a linear relationship between square period and absorption is revealed as shown in Figure 26.

Unlike the frequency shift caused by varying square size shown in Figure 14, variations in square period have minimal effect on the peak absorption frequency as shown in Figure 27. It is important to notice the difference in vertical scale size between these two figures.

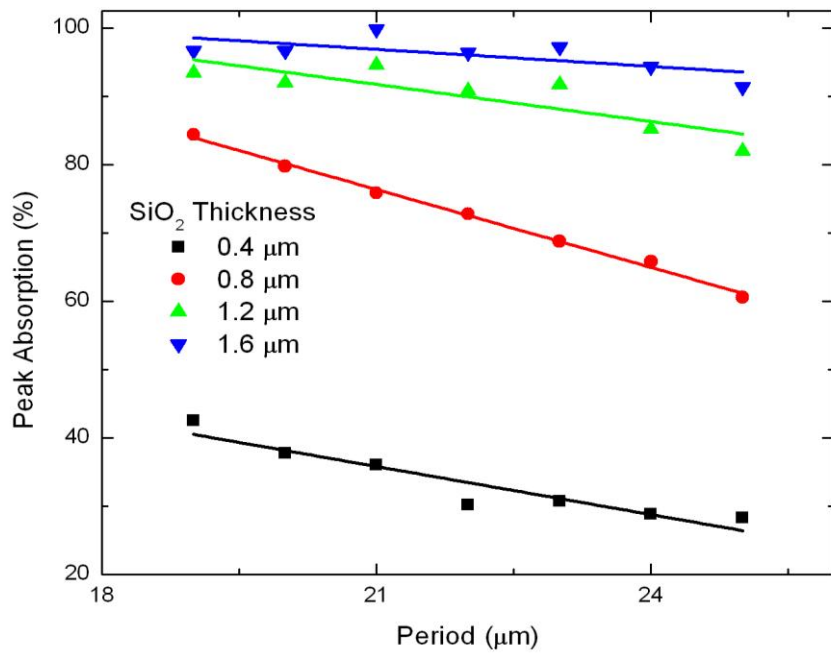


Figure 26. Peak absorption as a function of square period with constant square size of 16 μm . Data points are fitted with a linear fit.

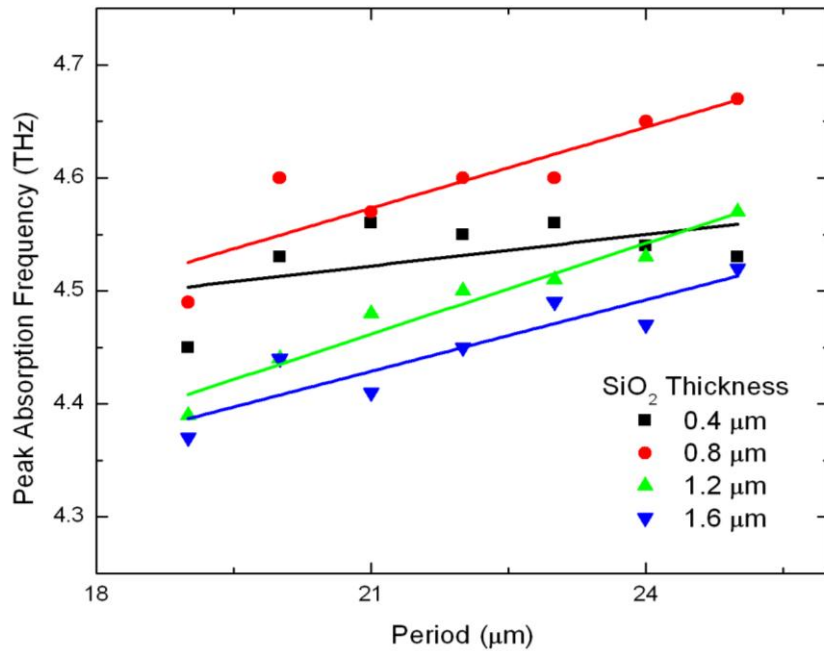


Figure 27. Peak absorption remains nearly constant as a function of square period with constant square size of 16 μm . Data points are fitted with a linear fit.

The final comparison of interest with regard to varying square period is the effect of fill factor on peak absorption as shown in Figure 28.

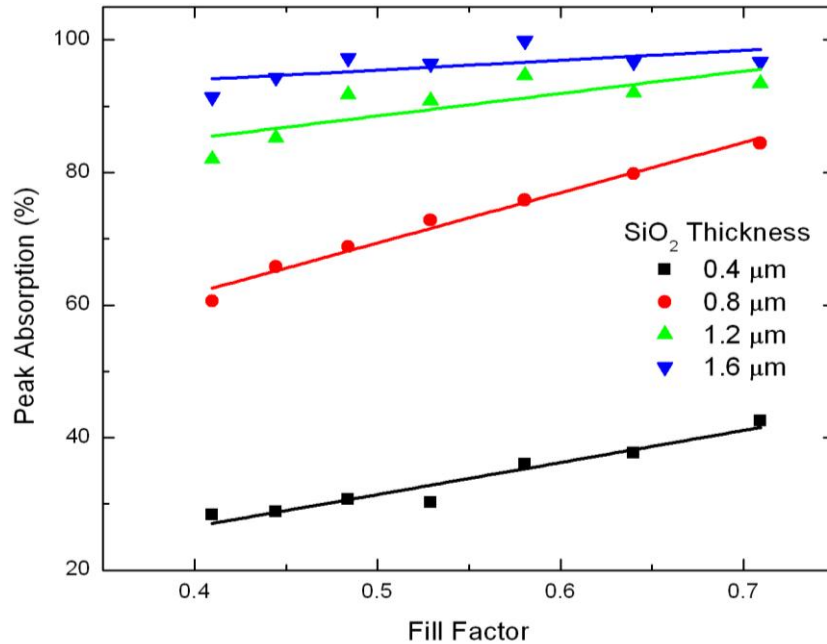


Figure 28. Peak absorption as a function of fill factor where square size remains constant at 16 μm . Data points are fitted with a linear fit.

As expected, fill factor demonstrates a consistent impact on peak absorption regardless of whether square period or square size is the parameter being adjusted as shown when comparing Figure 28 with Figure 19. Figure 28 matches very well to the linear portion of Figure 19, the region where fill factor is greater than 0.4. As the square period increases, fill factor decreases. As previously discussed, an increase in square period results in a decrease in absorption, so as expected, a decrease in fill factor correlates to a decrease in absorption. Notice that this effect reduces as the thickness of SiO_2 increases.

III. MODELING USING AN RLC CIRCUIT

A. RLC CIRCUIT ANALYSIS

While more sophisticated methods using finite element modeling are being used to understand the physics of these metamaterials, RLC circuits are also of interest due to their simplicity. The idea is to construct a series RLC circuit which models the behavior observed by the metamaterials with regard to THz absorption. In so doing, better understanding of the electromagnetic interactions within the metafilm can be gained along with insight into simplification of metafilm design. While there are various types of RLC circuits, the following analysis and discussion are with regard to an RLC circuit in series as shown in Figure 29.

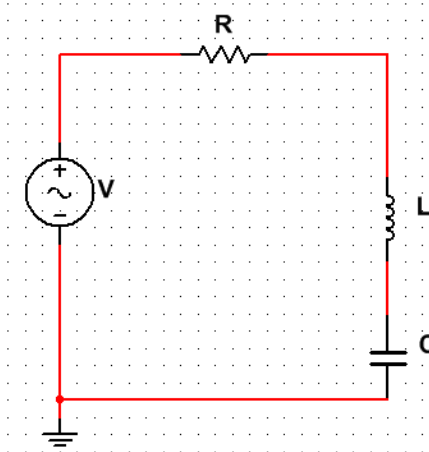


Figure 29. RLC circuit in series with resistance, R, inductance, L, and capacitance, C.

Both physical and behavioral analogies can be made between the metafilm and the RLC circuit. This helps to give a starting point in developing the RLC model and, conversely, allows for better understanding of the metafilm once an effective model is created. Since we are attempting to model the THz energy absorbed by the metafilm, the most logical circuit behavior to observe is power dissipated across the resistor. In this way, energy absorbed by the metafilm would be analogous to energy dissipated by the resistor. Modeling this behavior is achieved by simulating an alternating current (AC) frequency sweep with the RLC circuit and plotting the power dissipation for the range of

frequencies. The effectiveness of the model is determined by how well this plot compares to the THz absorption curves, originally shown in Figure 11.

The RLC circuit responds differently depending on the frequency of the oscillating current driving the circuit. The L and C values determine the resonance frequency, while resistance determines the power dissipated by the circuit. The peak power dissipation occurs at resonant frequency and decreases as the frequencies move away from resonance. The rate of this decrease depends upon the ratio of R to L. In this manner, there is an associated power dissipation curve for a series RLC circuit which peaks at the resonant frequency. The following relationships describe the behavior of this curve:

Power dissipated is related to current and resistance by the equation:

$$P = I^2 R \quad (3.1)$$

Resonant frequency is again given by the equation:

$$\omega_0 = 1 / \sqrt{LC} \quad (3.2)$$

Where,

$$\omega_0 = 2\pi f \quad (3.3)$$

Amplitude at the resonant frequency is given by:

$$P_{\max} = V^2 / R \quad (3.4)$$

The full width half maximum is given in radians per second:

$$\Delta\omega = R / L \quad (3.5)$$

By using these equations, the physical analogies between the RLC circuit and the metafilm emerge as the following questions are asked: (1) How does the dielectric thickness of the metafilm relate to capacitance, inductance, and resistance? (2) How does varying metafilm square size relate to varying capacitance, inductance, and resistance? (3) Does a change in metafilm fill factor correlate to a corresponding change in resistance? The next section explores the answers to these questions, revealing the analogies and insight that come forth from such comparisons and justifying the use of a series RLC circuit to model metafilm absorption.

B. RLC MODEL IMPLEMENTATION AND COMPARISON

Applying Equations 3.1 through 3.5 quickly reveals whether an RLC circuit is able to effectively model the absorption characteristics of these metafilms. By setting the values of R , L , and C in accordance with Equations 3.1 to 3.5, the peak absorption, FWHM, and resonant frequency were successfully modeled as shown in Figure 30. The AC analysis module of the software Multisim 12.0 was used in simulating the RLC circuit.

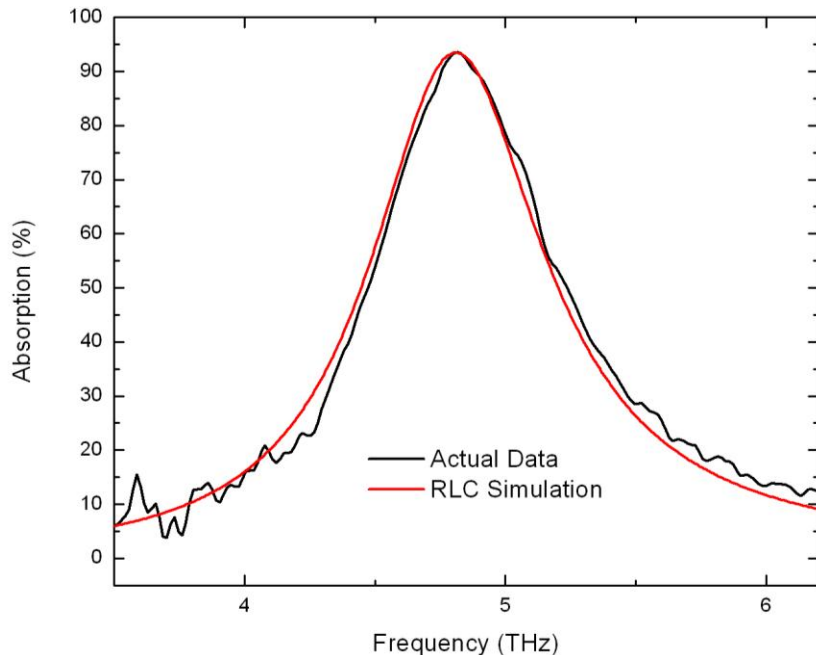


Figure 30. Comparison between an RLC circuit model (red) with $R = 1.07 \Omega$, $L = 0.21 \text{ pH}$, $C = 0.00521 \text{ pF}$ and actual data with Savitzky-Golay smoothing for a metafilm with square period of $21 \mu\text{m}$, square size of $15 \mu\text{m}$, and SiO_2 layer thickness of $1.2 \mu\text{m}$ (black line). RLC circuit simulated with voltage equal to 1 V.

Utilizing Equations 3.1 through 3.5 in conjunction with analysis from the data presented in section 2, the relationships between the metafilm and RLC circuit emerge.

1. Relating Capacitance to Square Size

As previously discussed, the relationship between square size and peak absorption frequency (Figure 15) suggests a relationship between capacitance (C) and square area (A) which may be explained by the parallel plate capacitance, $C = \epsilon A / d$. Since peak absorption frequency is dependent upon $1/\sqrt{LC}$ and demonstrates a linear relationship with inverse square size, the product LC must contain a factor of square size squared. The most straight forward explanation is that either L or C contains a factor of square size squared or both contain a factor of square size so that their product also contains a factor of square size squared. Based on the structure of the metafilm, it seemed most plausible that capacitance alone varied with square size. Since the metafilm contains two metallic plates separated by a dielectric, parallel plate models seemed the most logical in trying to describe the electromagnetic interactions at work. In this line of thinking, the parallel plate equation would describe capacitance, while the parallel bus bar equation would describe inductance [20].

The capacitance of a pixel in the metamaterial can be estimated using:

$$C = \epsilon A / d \quad (3.6)$$

Here, A is the area of the top metal square, ϵ is the dielectric constant of SiO_2 and d is SiO_2 thickness. The inductance per unit length can be estimated using the bus bar model as: [20]

$$L = \mu d / w \quad (3.7)$$

Here w is square size, μ is the magnetic permeability of SiO_2 , and d is SiO_2 thickness.

In applying the parallel plate equation, capacitance is dependent upon square size squared since this is the area of the top plate in the two plate model. Of course, this ignores the fact that the ground plane, the bottom plate, is larger than square size squared. In the same way the square area and ground plane are used in the parallel bus bar equation to determine inductance. Since the width and length of a square are the same, inductance should not depend upon square size, according to Equation (3.7), giving:

$$L = \mu d \quad (3.8)$$

Calculating the capacitance and inductance in this manner for a dielectric thickness of 1.2 μm , square size of 15 μm , $\epsilon = 3.54 \times 10^{-11} \text{ F/m}$, and $\mu = 1.26 \times 10^{-6} \text{ H} \times \text{m}^{-1}$ yields capacitance of $6.64 \times 10^{-15} \text{ F}$ and inductance of 1.51 pH. These values yield a resonant frequency of 1.59 THz, approximately one third of the experimental resonant frequency of 4.81 THz. Interestingly, when combined, the capacitance and inductance estimated using Equations 3.7 and 3.8 correctly predict the order of magnitude of the resonant frequency. However, this says little with regard to how accurate these equations are with regard to actual capacitance or inductance.

Using the calculated capacitance for the 15 μm square size and the experimental resonance frequency of 4.81 THz, the necessary inductance of 0.165 pH was calculated. Maintaining the notion that only capacitance depends upon square size, this inductance was held constant for the other metafilms of the same dielectric thickness and used in coordination with the varying square size capacitances to calculate the associated resonant frequencies in accordance with Equation 3.2. The inductance was calculated based on the 15 μm square size capacitance because that square size is near the middle and is found within the best fit of the data as seen in Figures 19 and 20. While yielding an accurate correlation to the experimental data, as shown in Table 1, this model simply captures the effect of square size on resonant frequency. Further discussion will show that this model cannot be used to predict absolute capacitance or relative change in capacitance of the actual metafilms.

Square Size (μm)	Capacitance (F) $C = \epsilon A / d$	Resonant Frequency (THz)		Difference (THz)
		Actual Data	Resonant Frequency (THz) RLC Simulation	
9	9.56E-15	7.85	8.02	0.17
10	8.53E-15	7.18	7.22	0.04
11	7.55E-15	6.55	6.56	0.01
12	6.64E-15	6.03	6.01	-0.02
13	5.78E-15	5.55	5.55	0.00
14	4.99E-15	5.19	5.15	-0.04
15	4.25E-15	4.81	4.81	0.00
16	3.57E-15	4.48	4.51	0.03
17	2.95E-15	4.24	4.24	0.00
18	2.39E-15	3.98	4.01	0.03

Table 1. Comparison of resonant frequencies for SiO_2 layer thickness of 1.2 μm with square period of 21 μm and varying square size.

2. Relating Resistance to Fill Factor

In Chapter II, a linear relationship between peak absorption percentage and inverse fill factor was revealed in Figure 20. Based on Equation 3.4, the peak power dissipation in the RLC circuit is proportional to $1/R$. This implies that there is a direct relationship between fill factor and resistance. As fill factor decreases, resistance increases and vice versa. This understanding allowed the derivation of an expression relating fill factor to resistance (where m_1 is the slope of the peak absorption vs. inverse fill factor line, m_2 is the slope of the peak absorption vs. inverse resistance line, and C is determined by the baseline resistance set by the experimental data):

$$R^{-1} = (m_1 / m_2) * \text{fillfactor}^{-1} + B \quad (3.9)$$

In order to match an RLC circuit curve to a metafilm absorption curve, a baseline resistance must be established. While there is a correlation between the resistance in the RLC circuit and the fill factor of the metafilm, it is difficult and perhaps even impossible to relate them to one another in an absolute sense. With this in mind, one approach is to choose an arbitrary starting point for resistance. For instance, in attempting to model the 15 μm square size, 1.2 μm thick dielectric metafilm, an arbitrary resistance value would be chosen and then normalized so that its peak corresponds to 93.5%, the peak absorption value of the experimental data. This arbitrary resistance value can then be inputted into R in Equation 3.9 to solve for B , from which all the other resistances for that dielectric thickness can be predicted based upon fill factor using Equation 3.9. As can be seen, Equation 3.9 is not helpful in determining an absolute resistance based upon fill factor; however, it is helpful in demonstrating how fill factor relates to resistance once a baseline has been established.

Another approach is to determine the baseline resistance based upon calculated inductance. If inductance is calculated first, then resistance can be calculated in accordance with Equation 3.5 so that the experimental FWHM is achieved. Using the fixed inductance necessary to support the parallel plate capacitance model in section 3-B1, this approach was applied successfully in modeling the absorption response of the 1.2 μm SiO_2 thickness metafilm as shown in Figure 31.

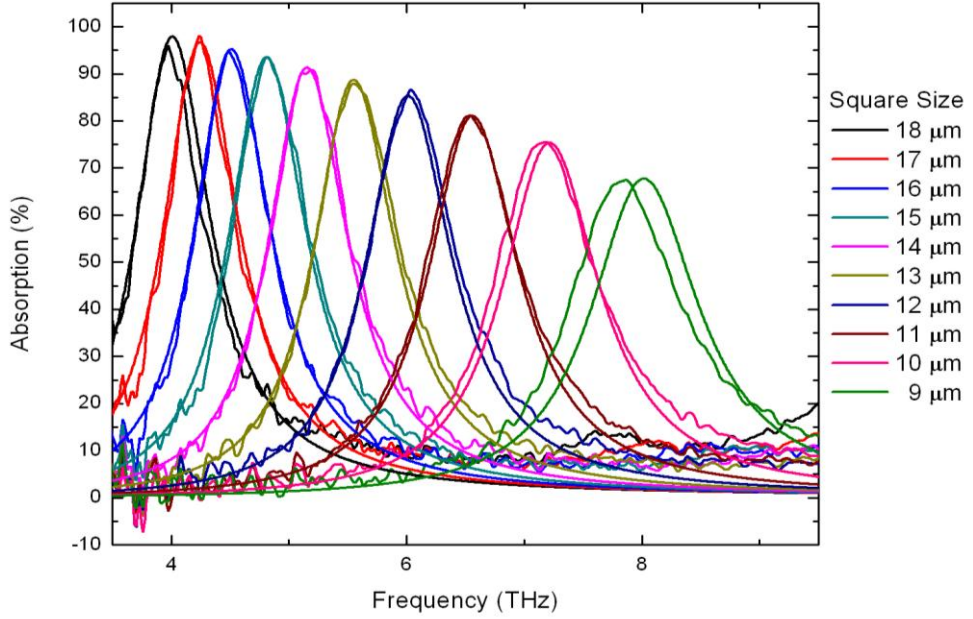


Figure 31. Comparison of RLC circuit model performance against actual data for a metafilm with square period of 21 μm , varying square size, and SiO_2 layer thickness of 1.2 μm . Smooth curves are given by the RLC circuit model.

In this case, inductance was held constant at 0.165 pH while capacitance varied according to the parallel plate equation calculations in Table 1. The slope (-7.3 absorption percentage / inverse fill factor) of the 1.2 μm dielectric in Figure 20 was used for m_1 . Based on an inductance of 0.165 pH and FWHM of 0.81 THz, the resistance value for the 15 μm square size, R_{15} , was determined to be 0.839Ω , using Equation 3.5. This necessitates a normalization factor of 78.49 Percent / W so that the resistance correlates to a peak absorption percentage of 93.5. Using Equation 3.2, where $V = 1\text{V}$ and $R_{15} = 0.839\Omega$, $P_{\max} = 1.191\text{W}$. Multiplying P_{\max} by the normalization factor, 78.49 Percent / W, yields the experimental absorption magnitude of 93.5%. In order to establish the slope, m_2 , an additional resistance value is needed. Since the 10 μm square size also falls on the best fit line in Figure 20, it serves as the best choice for which to establish m_2 . By taking the associated peak absorption percentage of 75.4 and dividing by the normalization factor of 78.49 Percent / W, P_{\max} was determined to be 0.9606 W, yielding R_{15} to be 1.041Ω . Plotting the peak absorption percentages, 93.5 and 75.4,

against their associated inverse resistances, $1/0.839 \Omega^{-1}$ and $1/1.041 \Omega^{-1}$, yields a line between the two points with m_2 determined by the equation (yielding $m_2 = 77.56$ absorption percentage / inverse resistance):

$$m_2 = (Peak_{15} - Peak_{10}) / (1/R_{15} - 1/R_{10}) \quad (3.10)$$

B is then estimated by substituting R_{15} , $fillfactor_{15}$, m_1 , and m_2 into Equation 3.9.

The other resistances were then determined based upon Equation 3.9, with Figure 31 demonstrating the result.

3. Relating Resistance to SiO_2 Thickness

Since resistance is directly related to peak absorption, Figure 13 is useful in finding a relationship between dielectric thickness and resistance. The absorption peaks in Figure 13 can be modeled by the equation (where x is SiO_2 thickness in μm and y is peak absorption percentage, and y_0, A and b are constants given by the exponential fit):

$$y = y_0 + Ae^{bx} \quad (3.12)$$

Combining Equation 3.12 with Equation 3.4 resistance should relate similarly:

$$1/R = 1/R_0 + ae^{bx} \quad (3.13)$$

Where the normalization factor, previously determined as 78.49 Percent / W, relates the constants as follows:

$$1/R_0 = y_0 / 78.49 \quad (3.14)$$

$$a = A / 78.49 \quad (3.15)$$

This was indeed found to be the case as the RLC model, using the resistance determined by Equation 3.13, performed closely to the experimental data with regard to peak absorption. This was achieved by using the constants from the exponential fit of the 13 μm data in Figure 13. This square size was chosen because its data points best fit the exponential curve. There $y_0 = 104.83$, $A = -151.177$, and $b = -1.80711$. Using Equations 3.14 and 3.15, $R_0 = 0.76815$ and $a = -1.90105$. Allowing x to equal 0.8, so that Equation 3.13 can be tested on the 0.8 μm SiO_2 thickness, the resistance for the 13 μm square size

with dielectric thickness 0.8 μm was computed as $R_{13} = 1.149 \Omega$, corresponding to an absorption magnitude of 68.3%. Experimental absorption for this metafilm is 69.0%, a difference of only 0.7%.

Taking it a step further, the same relationship (Equation 3.9) that was used to determine the resistances for the 1.2 μm thickness was used for the 0.8 μm thickness. Keeping m_1 and m_2 at -7.3 and 77.56 respectively, B to be used in Equation 3.9 was recalculated using the newly determined R_{13} . Based on this new B , Equation 3.9 was used to predict the resistances for all the square sizes on the 0.8 μm thick dielectric, with results matching very well with experimental absorption peaks as shown in Table 2.

Square Size (μm)	RLC Resistance (Ω)	Peak Absorption (%)	Peak Absorption (%)	Difference (%)
		RLC Simulation	Actual Data	
9	1.657	47.4	49.1	1.7
10	1.427	55.0	58.0	3.0
11	1.294	60.7	62.4	1.7
12	1.208	65.0	66.6	1.6
13	1.149	68.3	69.0	0.7
14	1.106	71.0	72.0	1.0
15	1.073	73.1	74.1	1.0
16	1.048	74.9	75.9	0.9
17	1.028	76.3	77.3	1.0
18	1.012	77.5	79.6	2.1

Table 2. Comparison of absorption peaks for SiO_2 layer thickness of 0.8 μm with square period of 21 μm and varying square size.

However, using the inductance required in accordance with the parallel plate capacitance model reveals a large discrepancy in FWHM. Applying the parallel plate capacitance model to the 0.8 μm SiO_2 thickness yields a capacitance of $9.956 \times 10^{-15} \text{ F}$ for the 15 μm square size. Calculating inductance so that FWHM yields the experimental result of 4.87 THz, requires $L = 0.1073 \text{ pH}$. Holding this inductance constant, the

FWHMs were computed for the varying resistances in Table 2. The discrepancy between the RLC model and the experimental data is shown in Table 3.

Square Size (μm)	RLC Resistance (Ω)	FWHM (THz) RLC Simulation	FWHM (THz) Actual Data	Difference (THz)
9	1.657	2.46	1.19	1.27
10	1.427	2.12	1.02	1.10
11	1.294	1.92	0.96	0.96
12	1.208	1.79	0.87	0.93
13	1.149	1.70	0.82	0.88
14	1.106	1.64	0.76	0.88
15	1.073	1.59	0.68	0.91
16	1.048	1.56	0.67	0.89
17	1.028	1.53	0.66	0.87
18	1.012	1.50	0.62	0.88

Table 3. Comparison of FWHM for SiO_2 layer thickness of 0.8 μm with square period of 21 μm and varying square size.

The model reveals a large discrepancy in FWHM, indicating that inductance and capacitance do not behave as predicted by the parallel plate capacitance model. According to that model, inductance should increase as SiO_2 thickness increases; however, for the FWHM and peak absorption modeled by the RLC circuit to match the experimental data, inductance must behave in a contradicting manner as revealed in Table 4.

SiO_2 Thickness (μm)	Capacitance Model Inductance (pH)	RLC Circuit Model Inductance (pH)
0.4	0.0537	0.4877
0.8	0.1071	0.2230
1.2	0.1650	0.1650
1.6	0.2300	0.1857

Table 4. Inductance required to support the parallel plate capacitance model compared to inductance required to support the RLC circuit model.

The resistance relationships are very effective in modeling the appropriate absorption peaks for both varying square size and SiO_2 thickness. If the RLC circuit is a comprehensive model, capable of explaining the absorption characteristics of the metafilms, then the necessary inductance to fit this model shows that simple parallel plate models cannot capture the complexities of these metafilms. For the RLC circuit to effectively model the metamaterial absorption characteristics, it is clear that inductance must decrease as SiO_2 thickness increases. This means that capacitance must increase while SiO_2 thickness increases in order for the resonant frequencies to correlate to the experimental absorption data. While it is not surprising that these complex metafilms cannot be adequately described by simple plate models, it is surprising that inductance and capacitance adjust with dielectric thickness in the opposite directions from which the plate models require.

4. RLC Circuit Values Necessary for Modeling Experimental Data

If the RLC circuit is an accurate model, as it seems to be, it is interesting to comparatively examine the R, L, and C values required to fit the experimental data. This was achieved by assuming a 1 V power source with 1 Ω resistance corresponding to 100% absorption. In other words, 1 W of power corresponds to 100% absorption by Equation 3.4. Using Equation 3.4 along with the experimental absorption data, the required resistance for each square size and SiO_2 thickness were computed as shown in Table 5 and depicted in Figure 32 and Figure 33. These values affirm the relationship between resistance in the RLC circuit and peak absorption by the metafilm as shown by comparing Figure 34 with Figure 20. Comparing Figure 13 to Figure 35 illustrates how $1/R$ is equivalent to peak absorption. Data throughout this section has either been fitted or plotted with connecting lines to better illustrate the trending behavior.

Square Size (μm)	SiO ₂ Thickness (μm)			
	0.4	0.8	1.2	1.6
9	4.53	2.04	1.49	1.25
10	3.99	1.73	1.33	1.12
11	3.72	1.60	1.23	1.08
12	3.28	1.50	1.15	1.03
13	3.17	1.45	1.14	1.04
14	3.03	1.39	1.10	1.06
15	2.97	1.35	1.07	1.02
16	2.77	1.32	1.06	1.00
17	2.49	1.29	1.02	1.00
18	2.48	1.26	1.04	1.01

Table 5. Resistance (Ω) necessary for RLC circuit to model experimental peak absorption data where 1 Ω corresponds to maximum absorption.

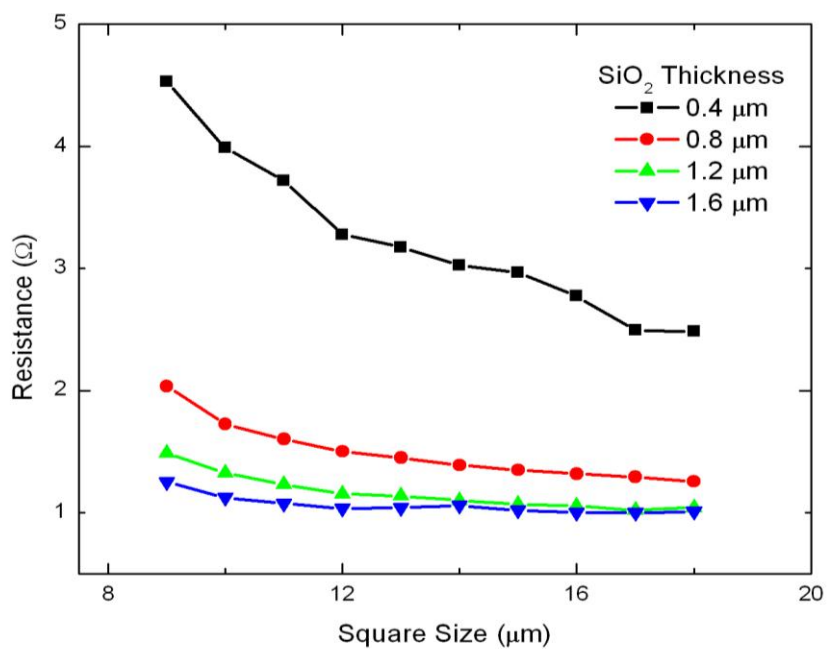


Figure 32. As a function of square size, resistance necessary for RLC circuit to model experimental peak absorption data where 1 Ω corresponds to maximum absorption.

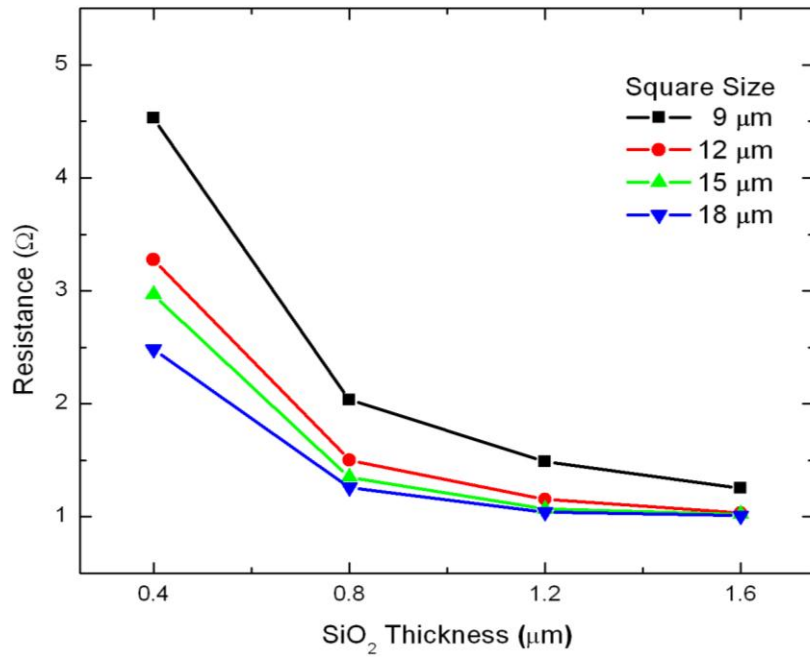


Figure 33. As a function of SiO_2 thickness, resistance necessary for RLC circuit to model experimental peak absorption data where 1Ω corresponds to maximum absorption.

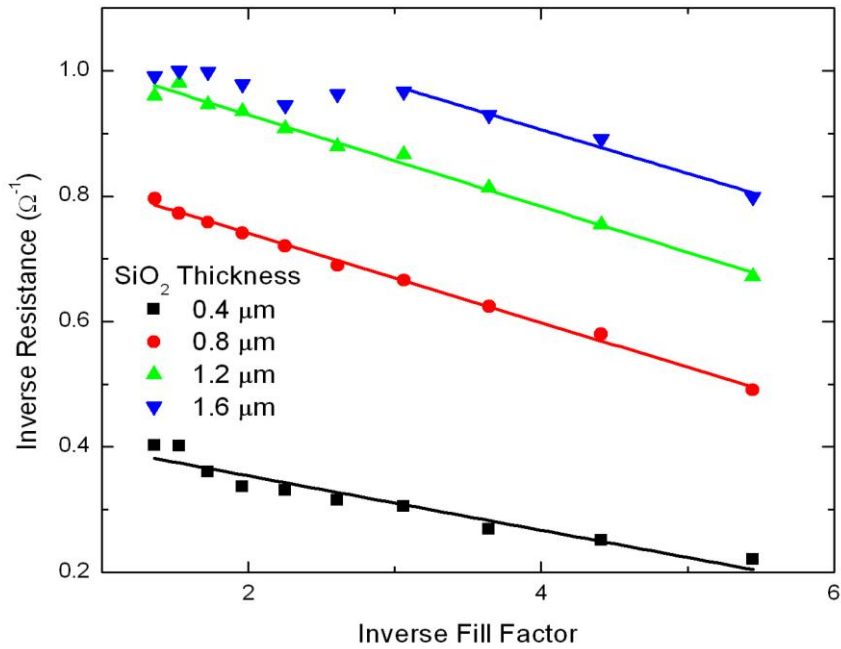


Figure 34. $1 / R$ as a function of $1 / \text{Fill Factor}$ fitted with a linear fit. Data points reaching near 100% absorption were not fitted since they obscure the linear relationship occurring below maximum absorption.

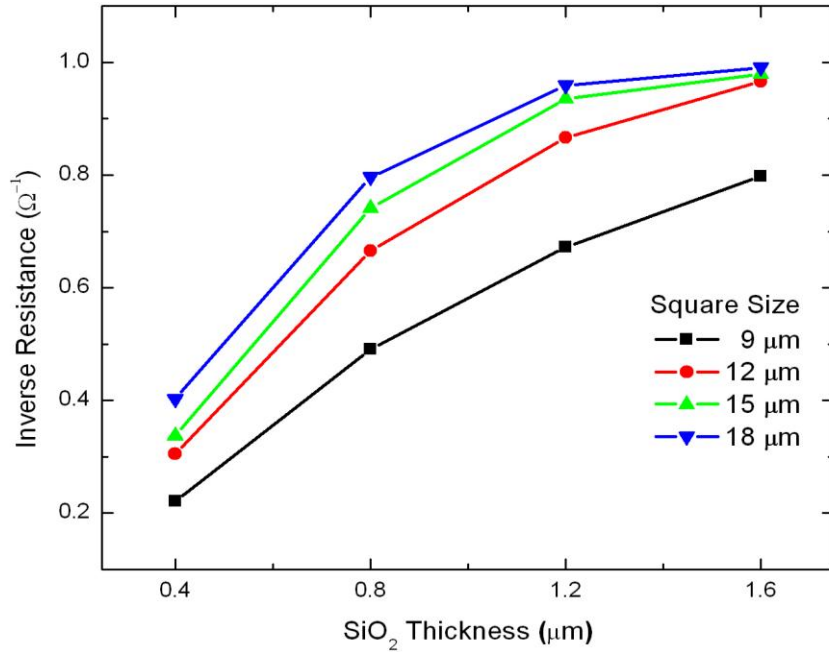


Figure 35. $1 / R$ as a function of SiO_2 thickness.

Based on the resistance calculations and Equation 3.5, inductance was calculated so that the FWHM of the RLC model matched the experimental data. The calculated values are shown in Table 6 and plotted in Figure 36.

Square Size (μm)	SiO ₂ Thickness (μm)			
	0.4	0.8	1.2	1.6
9	0.53	0.27	0.20	0.19
10	0.56	0.27	0.19	0.20
11	0.54	0.27	0.20	0.21
12	0.55	0.28	0.20	0.22
13	0.61	0.28	0.20	0.23
14	0.62	0.29	0.20	0.26
15	0.55	0.32	0.21	0.27
16	0.51	0.31	0.22	0.28
17	0.53	0.31	0.24	0.30
18	0.56	0.32	0.23	0.37

Table 6. Inductance (pH) necessary for RLC circuit to model experimental FWHM data given the baseline resistance calculated in Table 5.

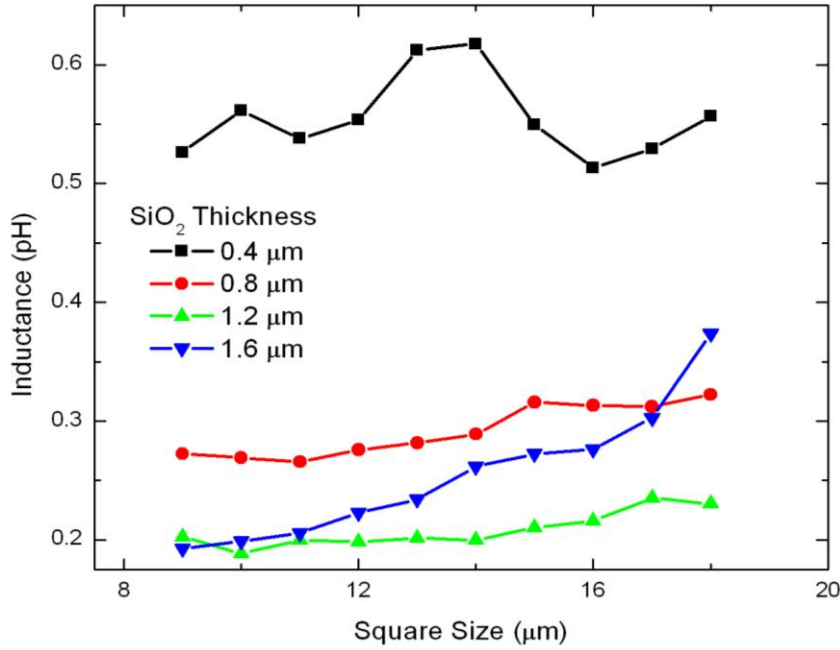


Figure 36. As a function of square size, inductance necessary for RLC circuit to model experimental FWHM data given the baseline resistance calculated in Table 5.

As revealed by Figure 36, inductance remains relatively constant for the smaller square sizes and then tends to increase as square size increases, especially in the case of the 1.6 μm thickness where inductance nearly doubles. It may be argued that there is a linear relationship between inductance and square size and that this is not so clear from the plot due to imperfections in the metafilm such as overetch. A linear relationship becomes slightly more visible when inductance is plotted against the square area, shown in Figure 37.

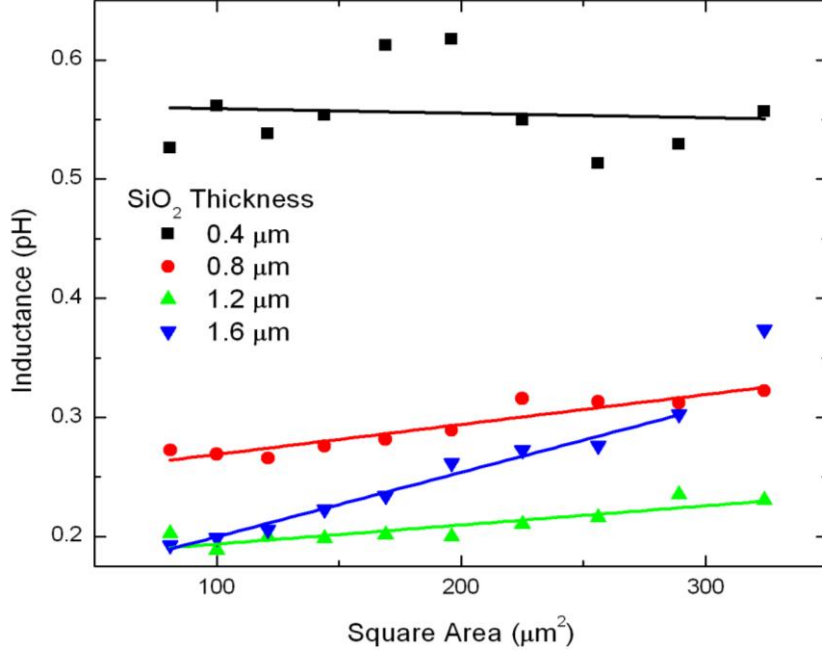


Figure 37. Necessary inductance as a function of square area, fitted with a linear fit, excluding the last data point in the 1.6 μm thickness.

Additionally, inductance tends to decrease while SiO_2 thickness increases, illustrated in Figure 38. This reemphasizes the relationship given in Equation 3.8 which contradicts the parallel bus bars model. The sudden increase in required inductance between the 1.2 and 1.6 μm thicknesses is most likely due to the saturated absorption occurring for the 1.6 μm thickness. Recall that Figure 34 shows that the resistance relationship with fill factor only works as long as maximum absorption has not been achieved. Once maximum absorption is achieved, the resistance must remain at 1Ω for the RLC curve to match the experimental data, though this may not be indicative of the actual interactions within the metafilm. If the resistance were allowed to decrease further once maximum absorption is achieved, it would necessitate a smaller inductance in order to maintain the appropriate FWHM in accordance with Equation 3.5. This helps to explain the behavior seen in Figure 38 and further indicates that the RLC circuit has bounds in which it can effectively model the metafilm absorption. Once maximum absorption is reached, the model becomes less effective.

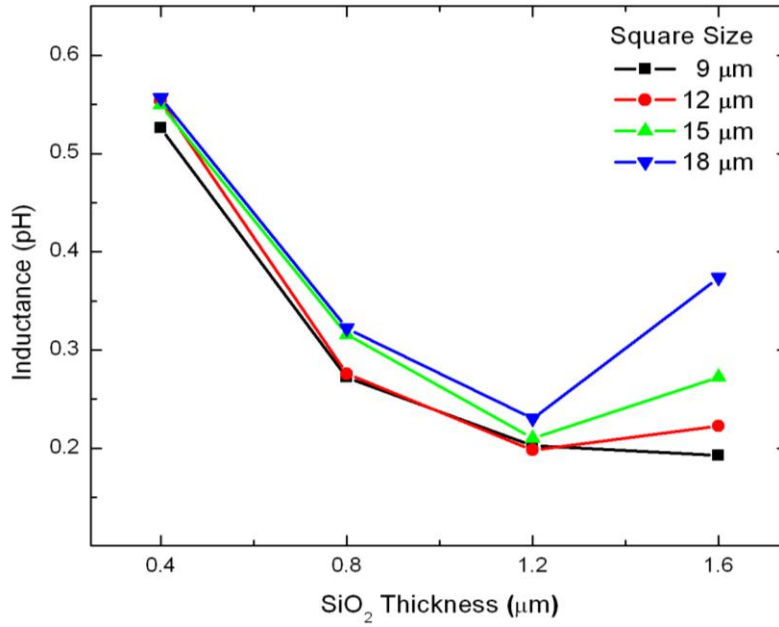


Figure 38. As a function of SiO₂ thickness, inductance necessary for RLC circuit to model experimental FWHM data given the baseline resistance calculated in Table 5.

Based on the inductance calculations and Equation 3.2, capacitance was calculated so that the resonant frequency of the RLC model matched the experimental data. These calculations are shown in Table 7 and plotted in Figure 39.

Square Size (μm)	SiO ₂ Thickness (μm)			
	0.4	0.8	1.2	1.6
9	0.75	1.48	2.03	2.30
10	0.88	1.80	2.61	2.69
11	1.09	2.15	2.96	3.07
12	1.23	2.42	3.51	3.33
13	1.38	2.87	4.07	3.70
14	1.56	3.21	4.71	3.80
15	1.98	3.38	5.21	4.14
16	2.37	3.87	5.85	4.71
17	2.68	4.31	5.99	4.93
18	2.84	4.65	6.94	4.41

Table 7. Capacitance (10^{-15} F) necessary for RLC circuit to model experimental resonant frequency data given the inductance calculated in Table 6.

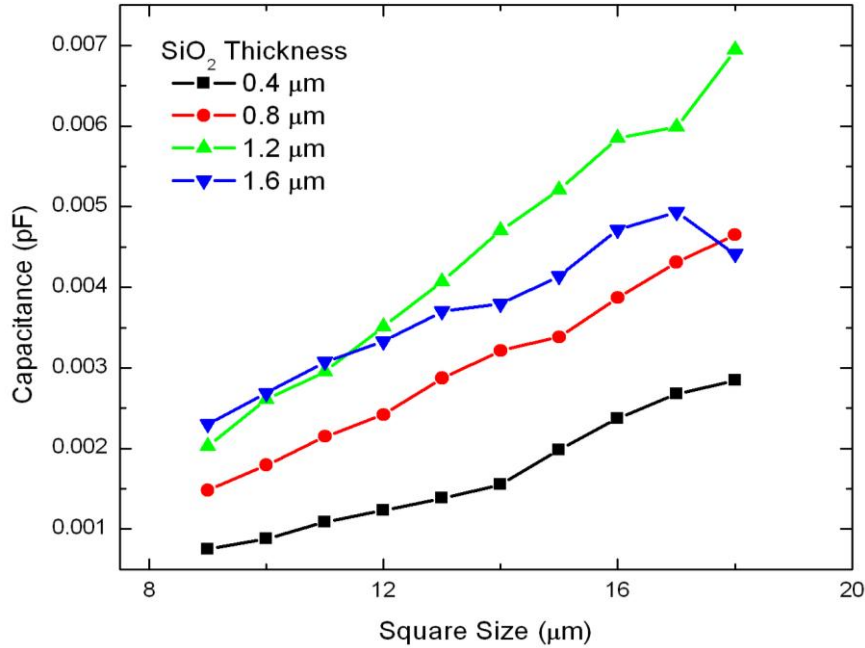


Figure 39. As a function of square size, capacitance necessary for RLC circuit to model experimental resonant frequency data given the inductance calculated in Table 6.

Interestingly, the data is nearly linear and becomes more so when capacitance is plotted against the square area, shown in Figure 40. While it was originally thought that the square area related to capacitance, as Figure 40 may suggest, the true relationship may be one in which both capacitance and inductance depend linearly upon square size. Then, the product of LC still exhibits a dependence on square area, as was demonstrated to be the case in the discussion regarding Figures 14 and 15.

Also of interest is that capacitance generally increases as SiO_2 thickness increases, contradicting the parallel plate model. This relationship is further illustrated in Figure 41. The inversion of the 1.6 μm and 1.2 μm thicknesses can be explained in the same way the sudden inductance increase with the 1.2 μm thickness was explained with regard to Figure 38. Since inductance is forced higher to compensate for the restraint on resistance at maximum absorption, capacitance is forced lower to maintain the appropriate FWHM.

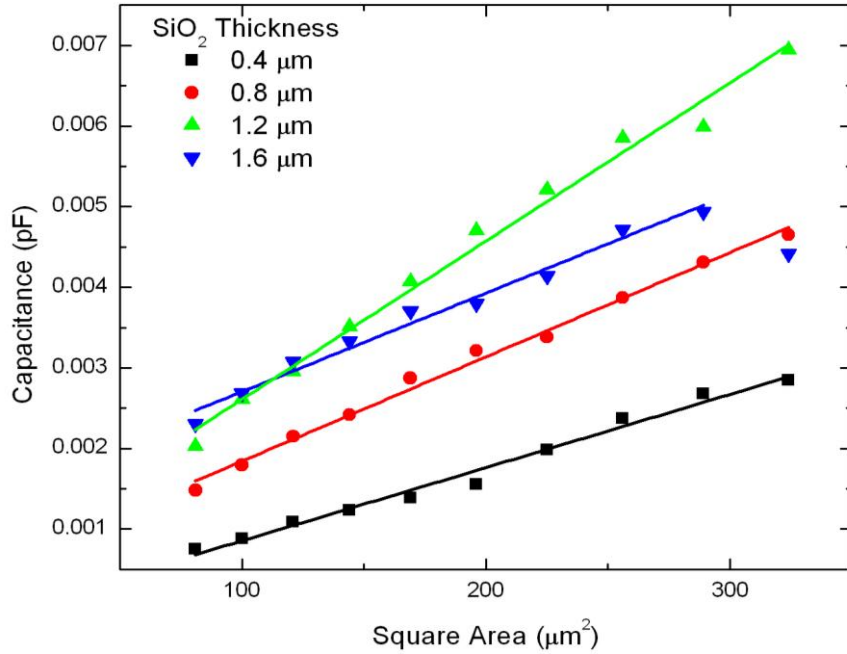


Figure 40. Necessary capacitance as a function of square area, fitted with a linear fit, excluding the last data point in the 1.6 μm thickness.

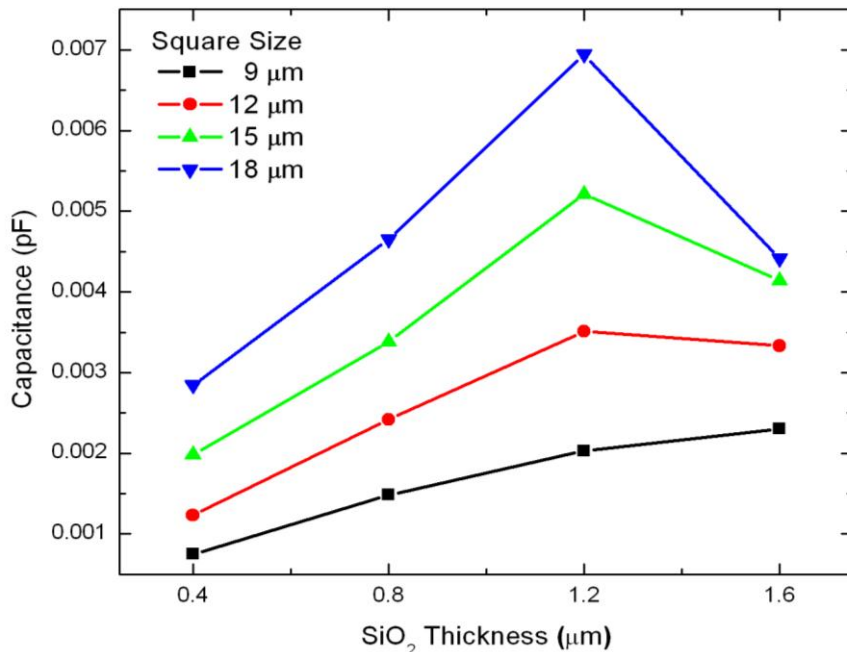


Figure 41. As a function of SiO_2 thickness, capacitance necessary for RLC circuit to model experimental resonant frequency data given the inductance calculated in Table 6.

C. RLC MODEL CONCLUSIONS

The RLC model confirms analysis from Chapter II, sheds new light on the possible electromagnetic interactions occurring within the metafilms, and reveals its own limitations. The model affirms that absorption and thus resistance directly relates to fill factor, showing that inverse resistance relates linearly to inverse fill factor. The model also affirms that square area relates to the product of inductance and capacitance; however, further study is necessary to determine the extent to which each of these factors relates to square size. Interestingly, while capacitance and inductance vary with dielectric thickness, their product changes very little, suggesting that dielectric thickness cancels or nearly cancels out when the product is taken. The capacitance and inductance required by the RLC model to match the experimental behavior are worth noting and deserve further investigation. The RLC model also proved that it has limitations once maximum absorption has been reached. With resistance no longer able to decrease according to its relationship with inverse fill factor, the inductance and, consequently, the capacitance were forced to compensate so that the RLC model matched experimental absorption. It is hard to believe that inductance and capacitance would actually behave in this manner as doing so goes against the trends for the rest of the data in Figures 38, 39, and 41.

IV. CONCLUSION

This research demonstrates that a series RLC circuit is able to effectively model the absorption characteristics of the metafilms. This should prove valuable in both the design and understanding of these metafilms. If inductance and capacitance in the RLC circuit directly relate to inductance and capacitance exhibited by the metafilms, then the RLC model may prove extremely beneficial in understanding these complexities. At the very least it gives a sense of how these parameters are changing with square size, square period, and SiO_2 thickness.

With regard to the effects square size and square period have on the absorption characteristics of a metafilm, increasing square size causes an increase in absorption magnitude and a decrease in absorption frequency, where this shift in frequency is dependent upon inverse square size. Increasing square period causes a decrease in absorption magnitude and a small increase in absorption frequency. While square size and square period both affect absorption magnitude, their relationship to one another, as defined by fill factor, is the most critical factor in achieving maximum absorption for a given SiO_2 thickness. Inverse fill factor relates linearly to absorption magnitude and demonstrates a direct relationship with resistance in the RLC model.

Resistance also showed a consistent relationship to SiO_2 thickness, though determining the correct equation to describe that relationship deserves further investigation. It was clearly observed that there is an ideal thickness depending upon fill factor and that the importance of thickness cannot be overlooked in metafilm design. As described in the introduction, the Fabry-Perot explanation for how metamaterials work may tie in with the resistance behavior observed for varying thicknesses. It could be that the thickness of the dielectric impacts the phase cancellation occurring within the Fabry-Perot effect. In this line of thinking, the resistance / thickness relationship should be fitted to a portion of the sine curve. This was done with some success, though it is just one possible explanation.

While this research certainly achieved its goal of better understanding how metafilm structure affects absorption magnitude and frequency, the mystery of understanding the electromagnetic interactions within the metafilms remains. From a physics standpoint, it would be of great interest to explore this further. It may also unlock more secrets in how to best design metamaterials.

Looking ahead to the application of these metafilms, it is encouraging to see the flexibility they offer in designing a sensor with specific absorption characteristics. With just three parameters—square size, square period, and dielectric thickness—sensitivity can be adjusted and tuned to a specific frequency with a desired bandwidth. With such high sensitivities and tunable frequency responses, it should be no surprise to see similar metafilms being used in commercial and military security applications as well as space based sensors in the near future. While there is still much to understand and improve upon, this may be the ground work for the high sensitivity THz sensors NASA desires for its future missions.

APPENDIX A

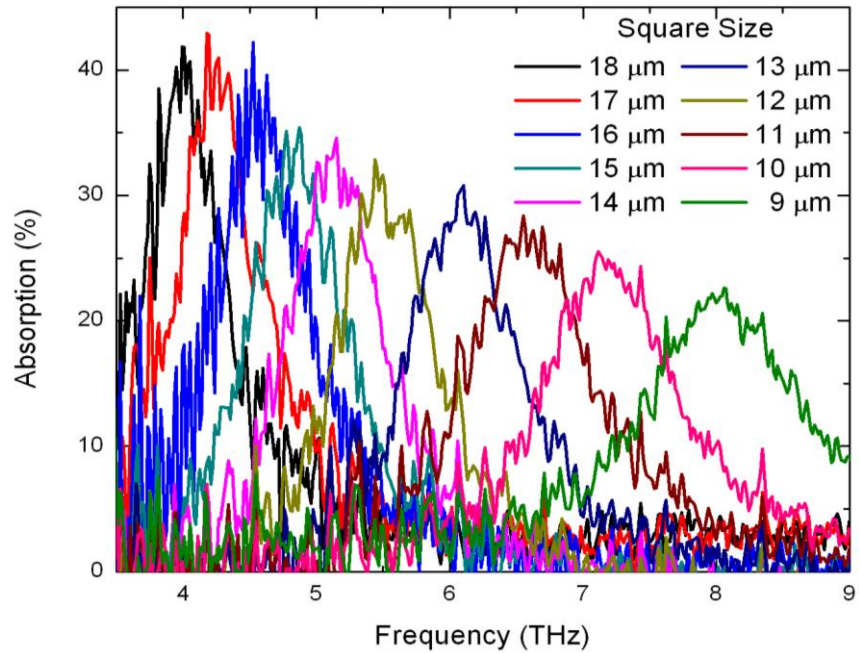


Figure 42. Raw data THz absorption of a metafilm with constant square period of 21 μm , varying square size, and SiO_2 layer thickness of 0.4 μm .

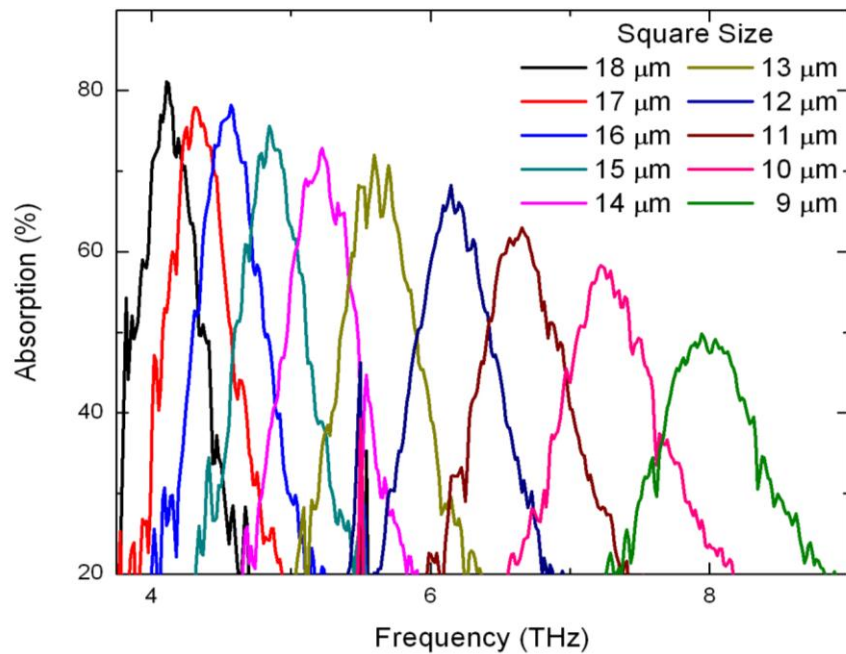


Figure 43. Raw data THz absorption of a metafilm with constant square period of 21 μm , varying square size, and SiO_2 layer thickness of 0.8 μm .

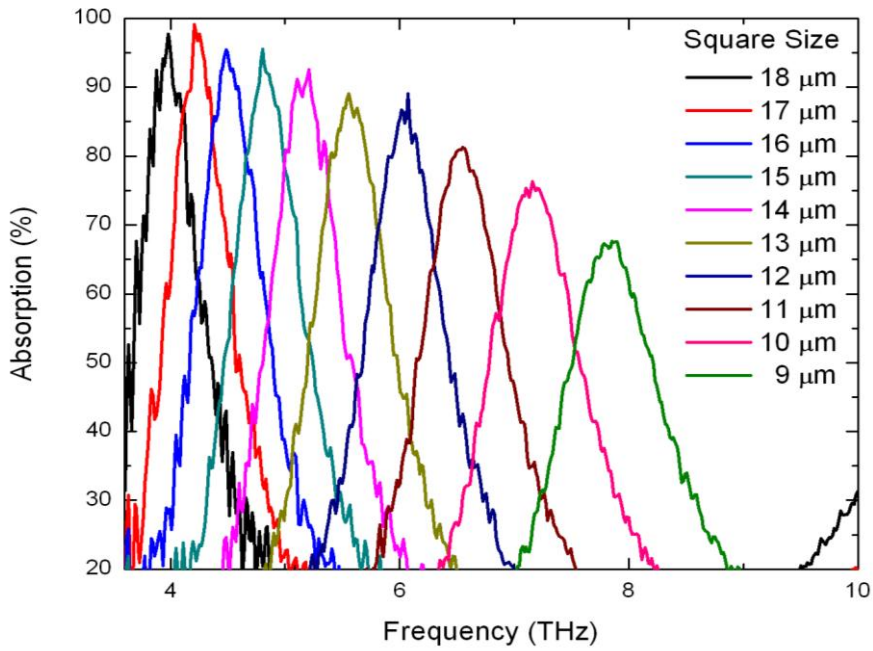


Figure 44. Raw data THz absorption of a metafilm with constant square period of 21 μm , varying square size, and SiO_2 layer thickness of 1.2 μm .

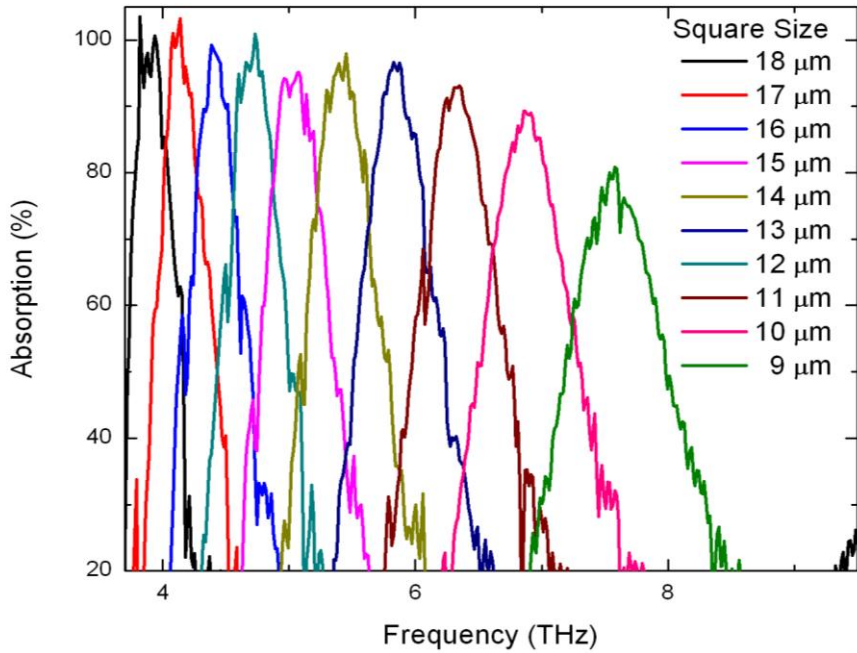


Figure 45. Raw data THz absorption of a metafilm with constant square period of 21 μm , varying square size, and SiO_2 layer thickness of 1.6 μm .

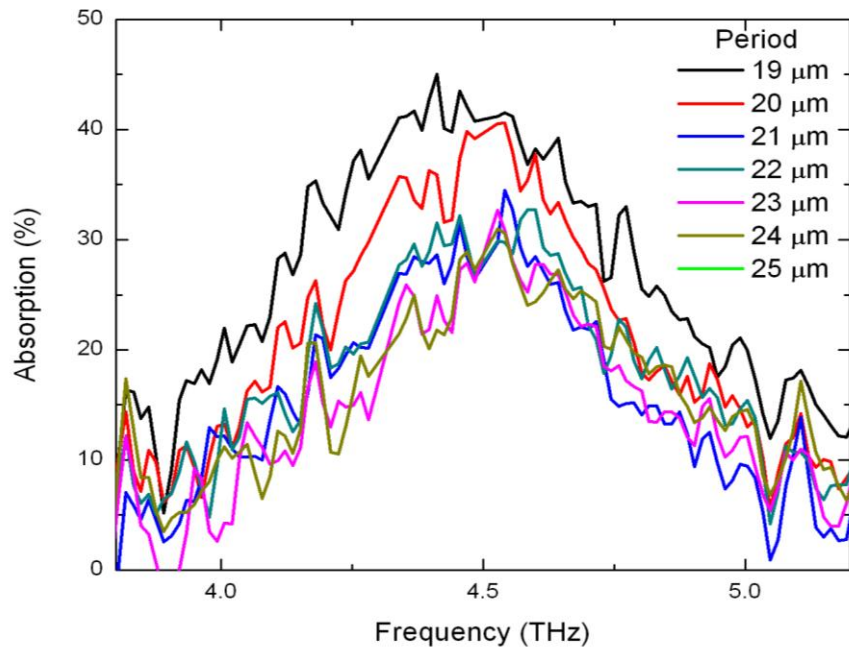


Figure 46. Raw data THz absorption of a metafilm with varying square period, constant square size of 16 μm , and SiO_2 layer thickness of 0.4 μm .

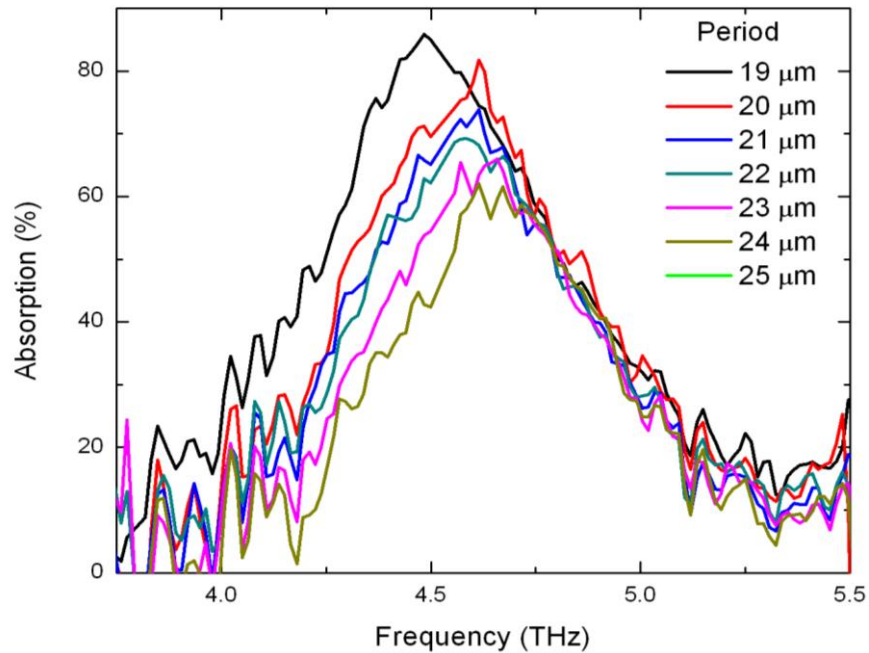


Figure 47. Raw data THz absorption of a metafilm with varying square period, constant square size of 16 μm , and SiO_2 layer thickness of 0.8 μm .

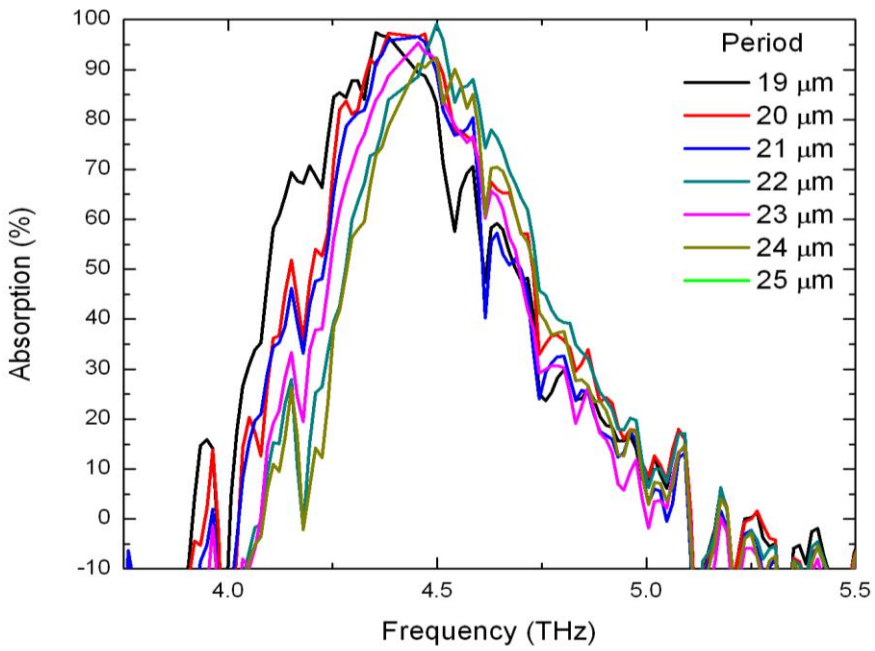


Figure 48. Raw data THz absorption of a metafilm with varying square period, constant square size of 16 μm , and SiO_2 layer thickness of 1.2 μm .

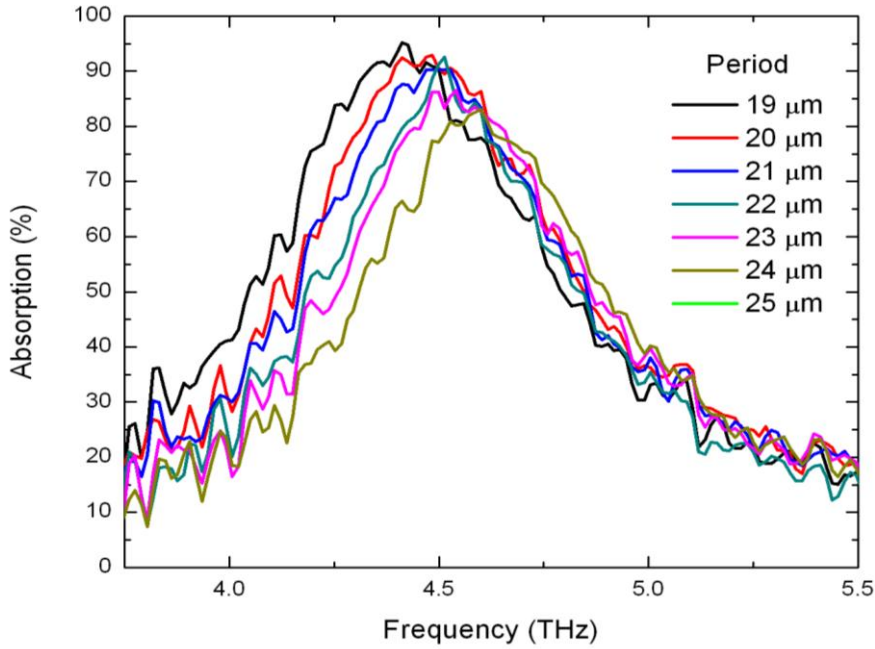


Figure 49. Raw data THz absorption of a metafilm with varying square period, constant square size of 16 μm , and SiO_2 layer thickness of 1.6 μm .

LIST OF REFERENCES

- [1] H. Tao, W.J. Padilla, X. Zhang, and R.D. Averitt, “Recent progress in electromagnetic metamaterial devices for terahertz applications,” *IEEE Journal of Selected Topics in Quantum Electronics*, vol. 17, no.1, pp. 92–101, Jan.-Feb. 2011.
- [2] D. Johnson “Metamaterials make physics seem like magic,” *Multiphysics Simulation, Special Advertising Section to IEEE Spectrum*, pp. 3–7, June 2012.
- [3] F. Alves, B. Kearney, D. Grbovic, N.V. Lavrik, and G. Karunasiri, “Strong terahertz absorption using SiO₂/Al based metamaterial structures,” *Appl. Phys. Lett.* 100, 111104, 2012.
- [4] F. Alves, B. Kearney, D. Grbovic, and G. Karunasiri, “Narrowband terahertz emitters using metamaterial films,” *Opt. Express* 20, 21025–21032, 2012.
- [5] L. Huang, D.R. Chowdhury, S. Ramani, M.T. Reiten, S. Luo, A.J. Taylor, and H. Chen, “Experimental demonstration of terahertz metamaterial absorbers with a broad and flat high absorption band,” *Opt. Lett.* 37, 154–156, 2012.
- [6] I. Hosako, N. Sekine, M. Patrashin, S. Saito, K. Fukunaga, Y. Kasai, P. Baron, T. Seta, J. Mendrok, S. Ochiai, H. Yasuda, “At the dawn of a new era in terahertz technology,” *Proceedings of the IEEE*, vol. 95, no. 8, pp. 1611–1623, Aug. 2007.
- [7] B. N. Behnken, G. Karunasiri, D. R. Chamberlin, P. R. Robrish, and J. Faist, “Real-time imaging using a 2.8 THz quantum cascade laser and uncooled infrared microbolometer camera,” *Opt. Lett.* 33, 440–442, 2008.
- [8] Tonouchi, Masayoshi, “Cutting-edge terahertz technology,” *Nat Photon*, vol.1, no. 2, pp. 97–105, Feb. 2007.
- [9] A. Rahman, A. K. Rahman, “Terahertz technology enables systems for molecular characterization,” *Laser Focus World*, vol. 48, no. 1, pp. 113–117, Jan 2012.
- [10] M. H. Arbab, T. C. Dickey, D. P. Winebrenner, A. Chen, M.B. Klein, and P.D. Mourad, “Terahertz reflectometry of burn wounds in a rat model,” *Biomed. Opt. Express* 2, 2339–2347, 2011.
- [11] C. M Armstrong, “The truth about terahertz,” *IEEE Spectrum*, vol. 49, no. 9, pp. 36–41, September 2012.
- [12] M. J. Fitch, R. Osiander, “Terahertz waves for communications and sensing” *Johns Hopkins APL Technical Digest*, vol. 25, no. 4, pp. 348–355, Oct.–Dec. 2004.

- [13] P. H. Siegel, “Terahertz technology,” *IEEE Transactions on Microwave Theory and Techniques*, vol.50, no.3, pp. 910–928, Mar 2002.
- [14] C. K. Walker, C. E. Groppi, “Introduction to the special section on 22nd international symposium on space terahertz technology,” *IEEE Transactions on Terahertz Science and Technology*, vol. 2, no.1, pp. 10–11, Jan. 2012.
- [15] P. H. Siegel, “THz applications for outer and inner space,” *Electromagnetic Compatibility, 2006. EMC-Zurich 2006. 17th International Zurich Symposium on*, vol., no., pp. 1–4, Feb. 27 2006–March 3 2006.
- [16] C. Kulesa, “Terahertz spectroscopy for astronomy: from comets to cosmology,” *IEEE Transactions on Terahertz Science and Technology*, vol. 1, no.1, pp. 232–240, Sept. 2011.
- [17] E. R. Mueller, R. Henschke, W. E. Robotham, L. A. Newman, L. M. Laughman, R.A. Hart, J. Kennedy, H.M. Pickett, “Terahertz local oscillator for the microwave limb sounder on the aura satellite,” *Appl. Opt.* 46, 4907–4915, 2007.
- [18] J. L. Buckner, L. May, “NASA investments in in situ technologies and instruments for sample return missions,” *2011 IEEE Aerospace Conference*, pp. 1–6, 5–12 March 2011.
- [19] F. Alves, D. Grbovic, B. Kearney, and G. Karunasiri, “Microelectromechanical systems bimaterial terahertz sensor with integrated metamaterial absorber,” *Opt. Lett.* 37, 1886–1888, 2012.
- [20] J. K. Orfanidis. (2010, November 13). *Electromagnetic Waves and Antennas: Chapter 10: Transmission Lines* [Online]. Available: <http://www.ece.rutgers.edu/~orfanidi/ewa/>.

INITIAL DISTRIBUTION LIST

1. Defense Technical Information Center
Ft. Belvoir, Virginia
2. Dudley Knox Library
Naval Postgraduate School
Monterey, California
3. Andres Larraza
Naval Postgraduate School
Monterey, California
4. Gamani Karunasiri
Naval Postgraduate School
Monterey, California
5. Fabio Alves
Naval Postgraduate School
Monterey, California
6. James Newman
Naval Postgraduate School
Monterey, California
7. Rudolf Panholzer
Naval Postgraduate School
Monterey, California
8. Dragoslav Grbovic
Naval Postgraduate School
Monterey, California
9. Brian Kearney
Naval Postgraduate School
Monterey, California
10. Alan Scott
Naval Postgraduate School
Monterey, California
11. Allan Phillips
Naval Postgraduate School
Monterey, California